

Mapping the Thermal Inertia of Phobos using Thermal Infrared Spectra  
and Thermophysical Modeling

By Nathan M. Smith

A Thesis

Submitted in Partial Fulfillment  
of the Requirements for the Degree of  
Master of Science  
in Applied Physics

Northern Arizona University

August 2018

Approved:

Christopher S. Edwards, Ph.D., Chair

Michael Mommert, Ph.D.

David E. Trilling, Ph.D.

# ABSTRACT

## MAPPING THE THERMAL INERTIA OF PHOBOS USING THERMAL INFRARED SPECTRA AND THERMOPHYSICAL MODELING

NATHAN M. SMITH

We present a map of the thermal inertia of Phobos, the larger of Mars' two moons, based on observations collected by Mars Global Surveyor (MGS) using the Thermal Emission Spectrometer (TES) instrument. We compare these observations with an existing airless body thermophysical model that was modified for Phobos. By comparing brightness temperature spectra derived from our TES observations with simulated spectra generated by our thermophysical model, we can constrain the thermal properties of Phobos' surface. One such property, thermal inertia, describes how well a surface resists changes in temperature over time. Thermal inertia is controlled by the physical characteristics of that surface, such as the particle size.

Using 10  $\mu\text{m}$  measurements, we derive an average thermal inertia of  $42.0 \pm 13.6 \text{ J m}^{-2} \text{ K}^{-1} \text{ s}^{-1/2}$  for the observed region, with local variations ranging from  $\sim 20 - 60 \text{ J m}^{-2} \text{ K}^{-1} \text{ s}^{-1/2}$ . This is similar to the  $\sim 50 \text{ J m}^{-2} \text{ K}^{-1} \text{ s}^{-1/2}$  thermal inertia of lunar regolith, composed primarily of fine dust.

The observations used in this work cover roughly one hemisphere of Phobos, centered on the trailing side of the moon as it orbits around Mars. Our results show a fairly uniform thermal inertia across the observed region, and are generally consistent with prior estimates that relied on disk-integrated observations and not the disk-resolved observations used in this work.

We provide a global description of the surface temperature of Phobos as it varies with time, applying our thermophysical model and assuming a uniform thermal inertia of  $42 \text{ J m}^{-2} \text{ K}^{-1} \text{ s}^{-1/2}$ . This provides mission planners with a robust characterization of the thermal

environment a spacecraft is likely to experience upon arrival at Phobos' surface.

## Acknowledgements

The author wishes to acknowledge the invaluable support of his committee members. It is through their expertise, advice, guidance, and encouragement that I have grown as a scholar and a scientist and without them, I could not have completed this work.

Christopher Edwards performed the initial work to identify the observation footprints for our TES observations. Michael Mommert developed our thermophysical model and performed the code modifications to adapt it to use with Phobos. Christopher Coffey and the team at NAU's High Performance Computing Center maintain the Monsoon computing cluster that provided the computational resources needed throughout this project.

Timothy Glotch of Stony Brook University made available the generous financial support which made this work possible, through a grant through the Remote In Situ and Synchrotron Studies for Science and Exploration (RIS4E) team under NASA's Solar System Exploration Research Virtual Institute (SSERVI).

The graduate students of NAU's Department of Physics and Astronomy, years past and present, have been a constant fount of magnanimity. Their collective contributions to the completion of this effort, as sounding-boards, listening ears, supportive shoulders, hospitable hosts, and subject experts are too numerous to list.

The author extends his deepest thanks and gratitude to all who have supported the completion of this project, materially, financially, emotionally, and otherwise.

# Contents

<b>1</b>	<b>Introduction</b>	<b>1</b>
1.1	Phobos . . . . .	1
1.2	Influences on the Thermal Environment of Phobos . . . . .	5
1.2.1	Mars Solar Longitude ( $L_s$ ) . . . . .	6
1.2.2	Local Solar Time (LST) . . . . .	8
1.3	Thermal Properties and Thermal Inertia . . . . .	8
1.4	Goal of this Thesis . . . . .	9
<b>2</b>	<b>History of Infrared Observations of Phobos</b>	<b>10</b>
2.1	Mariner 9 . . . . .	11
2.2	Viking . . . . .	12
2.3	Phobos 2 . . . . .	12
2.4	Mars Global Surveyor (MGS) . . . . .	13
2.5	Ground-based observations . . . . .	13
2.6	2001 Mars Odyssey (Odyssey) . . . . .	14
2.7	Mars Reconnaissance Orbiter (MRO) . . . . .	15
2.8	Mars Express (MEx) . . . . .	16
2.9	Future Missions . . . . .	17
2.10	Summary of Estimates of Thermal Properties . . . . .	18
<b>3</b>	<b>Observations</b>	<b>19</b>
3.1	Choice of Dataset . . . . .	19
3.2	Mars Global Surveyor Encounters with Phobos . . . . .	20
3.3	Thermal Emission Spectrometer (TES) . . . . .	24
3.4	Selection of Observations . . . . .	26
3.5	Summary of Observations . . . . .	27
<b>4</b>	<b>Model</b>	<b>31</b>
4.1	Model Description . . . . .	31
4.1.1	Illumination of facets . . . . .	32
4.1.2	Thermal Diffusion . . . . .	33
4.1.3	Surface Roughness . . . . .	35
4.1.4	Solving for Surface Temperature . . . . .	36

4.1.5	Calculation of Observed Flux . . . . .	37
4.1.6	Model Output . . . . .	38
4.2	Modifications to the Model . . . . .	39
4.2.1	Eclipsing . . . . .	39
4.2.2	Mars-Shine . . . . .	42
4.2.3	Phobos Shape Model . . . . .	45
4.2.4	Integration of Flux within FOV . . . . .	47
4.2.5	Geometry of Illumination Sources and Observer . . . . .	47
4.3	Model Iterations . . . . .	48
4.4	Derivation of Observed Thermal Inertia . . . . .	49
<b>5</b>	<b>Results</b>	<b>52</b>
5.1	Average Thermal Inertia of Phobos . . . . .	52
5.2	Mapping the Thermal Inertia of Phobos . . . . .	53
<b>6</b>	<b>Analysis and Discussion</b>	<b>57</b>
6.1	Analysis . . . . .	57
6.1.1	Local Solar Time Dependence of Thermal Inertia . . . . .	58
6.1.2	Wavelength Dependence of Thermal Inertia . . . . .	62
6.2	Limitations . . . . .	63
6.3	Physical Interpretation of Determined Thermal Inertia . . . . .	65
6.4	Thermal Environment of Phobos . . . . .	66
<b>7</b>	<b>Conclusions and Future Work</b>	<b>68</b>
7.1	Conclusions . . . . .	68
7.2	Future Work . . . . .	69
<b>A</b>	<b>Mars-Shine</b>	<b>77</b>
A.1	Overview . . . . .	77
A.2	Apparent size of Mars . . . . .	78
A.3	Mars global climate model . . . . .	81
A.4	Radiant intensity . . . . .	81
A.5	Statistical integration . . . . .	82
A.5.1	Selection of points . . . . .	83
A.5.2	Local time . . . . .	86
A.6	Results . . . . .	87

# List of Tables

1.1	Key Dates of Martian Seasons According to Mars $L_s$ . . . . .	6
2.1	Summary of Estimates of Phobos' Thermal Inertia . . . . .	18
3.1	Summary of Observations . . . . .	24
4.1	Surface Roughness Conditions . . . . .	36
5.1	Statistics of Thermal Inertia Distributions at Nine Wavelengths . . . . .	53

# List of Figures

1.1	Map of Phobos . . . . .	3
1.2	Context Map of Phobos . . . . .	4
1.3	Mars Solar Longitude . . . . .	7
3.1	Orbits of Phobos and MGS . . . . .	23
3.2	Map of Observation Coverage . . . . .	28
3.3	Sample TES Footprints . . . . .	30
4.1	Diurnal Temperature Curve of a Representative Facet . . . . .	40
4.2	Angular Size of Mars . . . . .	41
4.3	Diurnal Flux Curve Arriving at Phobos from Mars (Mars-Shine) . . . . .	44
4.4	Comparison of Shape Model to Tri-axial Ellipsoid . . . . .	46
4.5	Comparison of Modeled and Observed Brightness Temperature . . . . .	50
5.1	Histogram of Thermal Inertia . . . . .	54
5.2	Map of Thermal Inertia Across Phobos' Surface . . . . .	55
5.3	Map of Thermal Inertia Across Phobos' Surface . . . . .	56
6.1	Diurnal Temperature Curve at Phobos Equator near Perihelion . . . . .	59
6.2	Thermal Inertia vs Local Solar Time . . . . .	60
6.3	Thermal Inertia vs Local Solar Time across nine wavelengths . . . . .	61
6.4	Thermal Inertia vs Wavelength . . . . .	62
6.5	Diurnal Temperature Curve of a Representative Facet . . . . .	66
6.6	Map of Daily Temperature Extremes on Phobos near Perihelion . . . . .	67
A.1	Definition of Mars Angular Radius, $\theta$ . . . . .	79
A.2	Defining Solid Angle Subtended by Mars, $\Omega$ . . . . .	80
A.3	Selection of Random Points on Mars . . . . .	86
A.4	Longitudinally Averaged Mars-Shine Diurnal Curve . . . . .	88
A.5	Residuals from Longitudinally Averaged Mars-Shine Diurnal Curve . . . . .	89
A.6	Seasonal Variation in Infrared and Solar Mars-Shine . . . . .	90

# Dedication

*To Natalie, my fundamental constant.*

# Chapter 1

## Introduction

### 1.1 Phobos

Phobos is the larger of Mars' two moons. It is irregular in shape, with many mounds and craters deforming its surface. It extends  $\sim 26$  km along its longest axis, but along its rotational axis (its shortest) only reaches  $\sim 18$  km across (Willner et al., 2014). Based on estimates of its mass, Phobos appears to have a quite low density, only  $1876 \text{ kg/m}^3$ , indicating a porous interior with up to 30% porosity (Andert et al., 2010).

Phobos orbits Mars with a semimajor axis of 9378 km, only 2.76 Mars radii. This places Phobos only  $\sim 6000$  km above Mars' surface. It circles Mars every 7 hours 40 minutes, so fast, in fact, that from Mars' surface, Phobos rises in the West, passes overhead over a matter of a few hours, and sets in the East. Phobos' orbit is nearly perfectly equatorial, with an inclination relative to Mars' equator of only  $\sim 1^\circ$ , and nearly circular, with an eccentricity of 0.015. From Mars' surface, Phobos is only visible from latitudes equatorward of  $\sim 70^\circ$ . It rotates exactly once per orbit, as a result of tidal locking keeping the same hemisphere pointed toward Mars at all times.

Phobos was discovered by Asaph Hall on August 18, 1877, at the US Naval Observatory

in Washington, DC, (Hall, 1878). Its close proximity to Mars had made it—as well as Mars’ smaller moon, Deimos—difficult to observe. Over 140 years later, our understanding of Phobos has grown considerably, with many observations collected by spacecraft sent to study Mars. However, no mission has successfully been sent specifically to investigate Phobos.

The origin of Phobos has been in question since its discovery. Hall (1877) asked if Mars might have “picked up a couple of very large meteorites, which have approached him closely?” This idea, that Phobos and Deimos were captured asteroids that wandered in from the Main Belt, gained considerable traction as spectra collected from the moons displayed marked similarity to C- and D-type asteroids. However, as suggested as early as Hall (1877), the tight, equatorial, and nearly circular orbits of the two moons make this scenario suspect. An impact origin, similar to that of our own Moon, sees support in the community, though the exact circumstances are hotly debated.

Phobos’ surface is covered in a layer of dusty regolith, giving it a dark red color across most of its surface (Thomas et al., 2000). Phobos has a fairly low albedo, similar to that of C-type asteroids, varying across the surface from  $\sim 0.05 - 0.10$  in visible light (Fraeman et al., 2014). Spectroscopy and imagery reveal a region with a distinctly bluer coloration associated with Phobos’ largest crater, Stickney (Murchie & Erard, 1996) This “blue unit” stands in contrast to the “red unit” covering the rest of the moon. Available spectra of each of these units are notable for their lack of spectral absorption features, and as such, their composition remains ambiguous (Pieters et al., 2014).

Over time, meteoroids impact Phobos’ surface, breaking rocks down into smaller particles in a process known as impact gardening. The more uniform Phobos’ surface is, the older it must be, as the process of impact gardening must take time to occur. Coarser particles would imply a younger surface. Likewise, a surface with large variations in particle size would imply a younger surface, as over time the surface would become uniformly saturated with fine dust. By measuring the thermal inertia of Phobos, a proxy for particle size, and

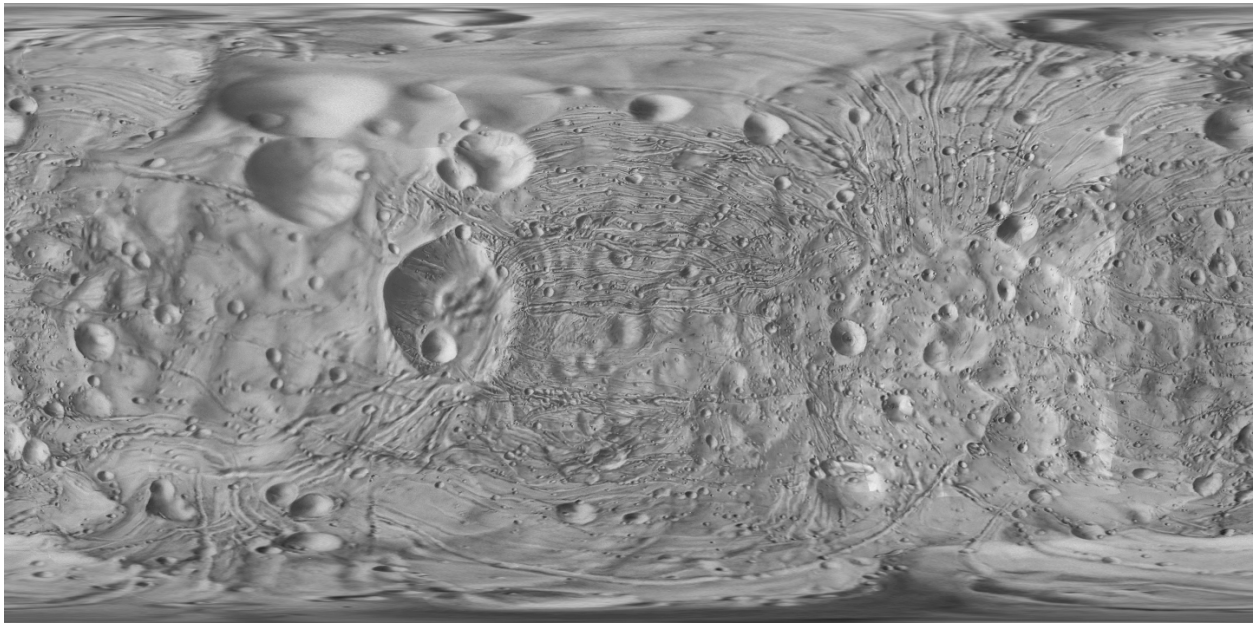


Figure 1.1 Map of Phobos, centered on the sub-Mars hemisphere. Based on the Stooke (2015) small bodies map set (PDS Data Set ID: MULTI-SA-MULTI-6-STOOKEMAPS-V3.0). Note Stickney crater, just left of center. This rectangular projection severely distorts the irregular shape of Phobos, particularly near the poles, causing circular craters to appear squashed and stretched.

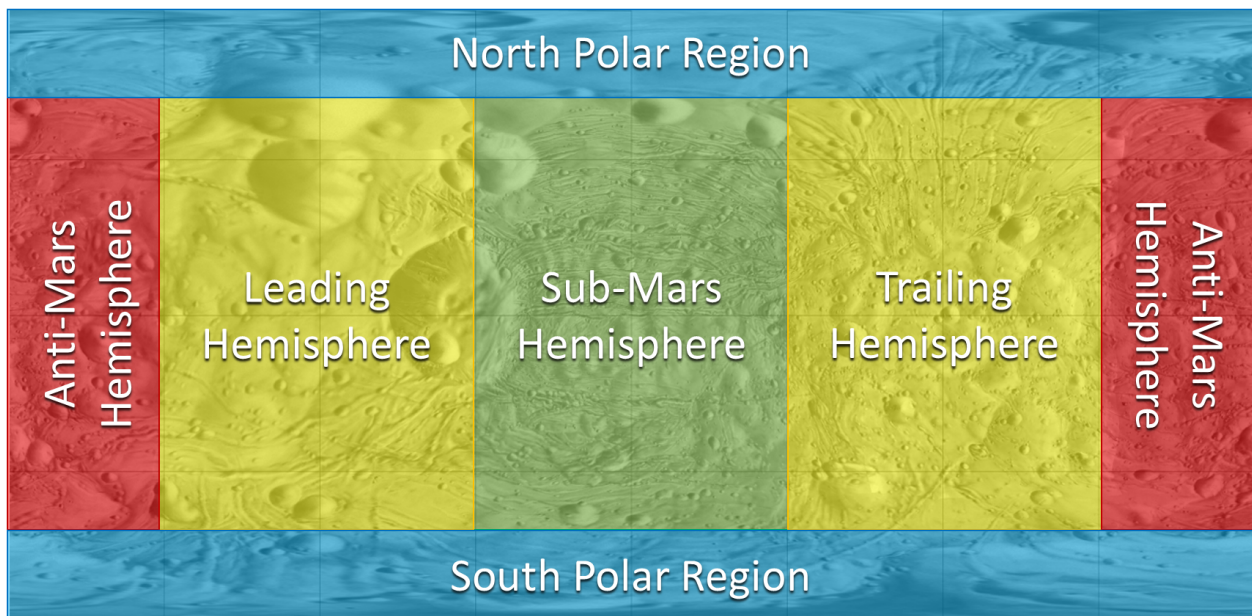


Figure 1.2 Map of Phobos, labeling the different hemispheres. The sub-Mars hemisphere, in green, is centered, making the anti-Mars hemisphere, in red, wrap across the left and right margin. Phobos orbits prograde, making the leading hemisphere to the west of the sub-Mars hemisphere, and the trailing hemisphere to the east (both yellow). The polar regions (in blue) are found in the north and south, respectively.

mapping thermal inertia's variation across its surface, this investigation may help to resolve questions regarding Phobos' age and evolutionary history.

## 1.2 Influences on the Thermal Environment of Phobos

The temperature of a planetary surface ultimately depends on how much energy is absorbed by that surface over time, and how quickly it can radiate that energy away. The largest source of energy falling on Phobos' surface is the Sun, which at the orbit of Mars has an average irradiance, or energy flux, of  $\sim 586 \text{ W/m}^2$ . A small amount of energy also arrives at Phobos from Mars, a combination of reflected sunlight and thermal emission from Mars' surface. This contribution varies in strength, but never amounts to more than  $\sim 50 \text{ W/m}^2$ . Appendix A describes in detail the method used in this work to precisely quantify this effect, known as Mars-shine.

The amount of sunlight reaching a given part of Phobos' surface depends not only on the distance from the Sun to Phobos, but also the inclined angle that surface makes with respect to the incoming light. The more directly the sunlight falls onto the surface, the greater the energy absorbed per unit area, and so the warmer that surface becomes.

Both the distance from Phobos to the Sun and the angle of the incoming sunlight vary over each Martian year. The distance varies as a result of Mars' eccentric orbit ( $e = 0.0934$ ) carrying Phobos closer and further from the Sun. At aphelion, Phobos is 1.67 AU from the Sun, while at perihelion, Phobos is just 1.38 AU. The incidence angle of sunlight changes just as Earth's seasons change, due to Mars' tilted rotational axis with respect to the plane of its orbit. Phobos orbits Mars just above its equator, and is tidally locked to Mars as well. This means Phobos' rotational axis is essentially the same as Mars, so it experiences the same seasons as its parent planet. During northern summer, Phobos' north pole tilts towards the sun by  $\sim 25^\circ$ , and is illuminated for months on end. In northern winter, the

Table 1.1 Key dates in the Martian calendar,  $L_s$

$L_s$	Event
$0^\circ$	northern spring equinox
$17.45 - 28.76^\circ$	observations used in this work
$56.8^\circ$	end of northern spring eclipse season
$71^\circ$	aphelion
$90^\circ$	northern summer solstice
$120.9^\circ$	start of northern autumn eclipse season
$180^\circ$	northern autumn equinox
$244.1^\circ$	end of northern autumn eclipse season
$251^\circ$	perihelion
$270^\circ$	northern winter solstice
$300.4^\circ$	start of northern spring eclipse season

Note. — Phobos’ eclipse seasons are discussed in greater detail in Section 4.2.1 (Pratt & Hopkins, 2011).

north pole is tilted  $\sim 25^\circ$  away, and remains dark, receiving no sunlight.

### 1.2.1 Mars Solar Longitude ( $L_s$ )

To keep track of these seasonal variations, Mars scientists use a sort of calendar, reduced to a single number: Mars Solar Longitude, or  $L_s$ . This number tracks Mars’ progress around the Sun, as measured in degrees from Mars’ northern spring equinox. Table 1.1 gives a few key reference points for events throughout each Martian year, and, for context, Figure 1.3 illustrates these points in Mars’ orbit around the Sun.

$L_s$  does usefully describe the changing of Mars’ seasons; however, because Mars travels along its orbit more quickly the closer it is to the Sun,  $L_s$  does not change at a constant rate. The period from  $L_s = 0$  to  $L_s = 180$  takes about 75 sols (Martian solar days) longer than the period from  $L_s = 180$  to  $L_s = 360$ .

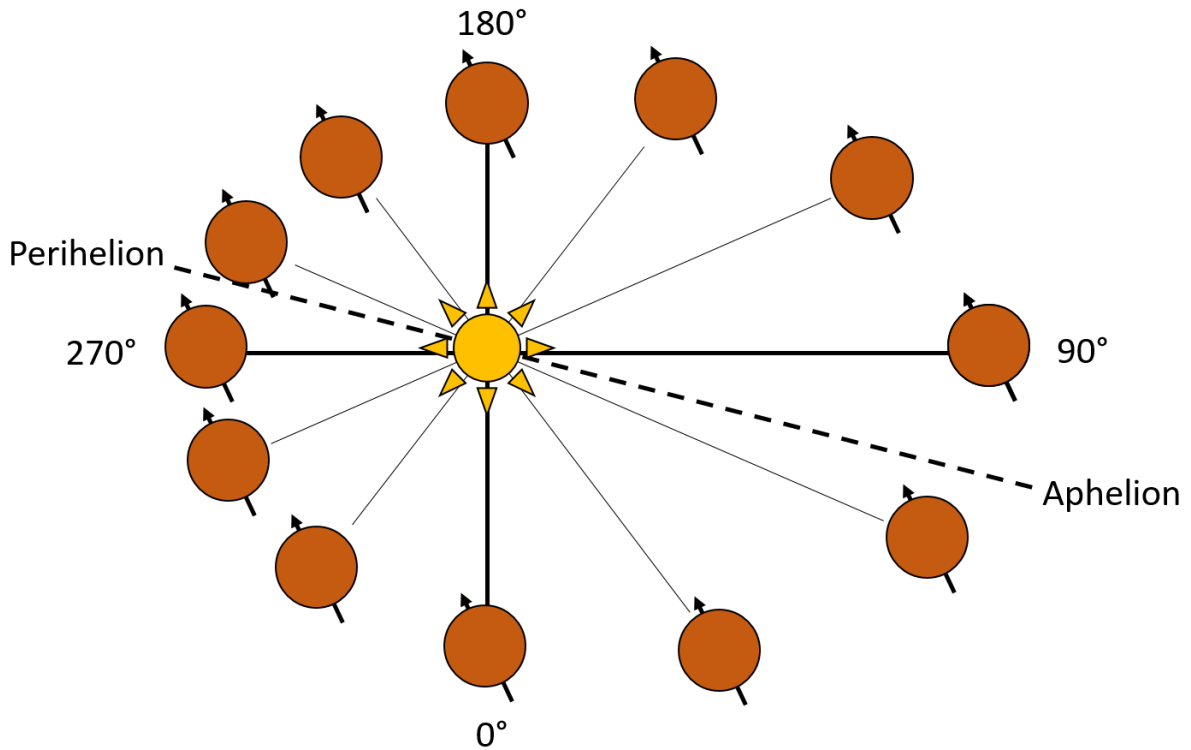


Figure 1.3 Mars' orbit around the Sun, illustrating Mars Solar Longitude ( $L_s$ ). Table 1.1 gives the description of key dates in the Martian year in terms of  $L_s$ . Several of these events are shown here, including perihelion and aphelion. Mars is shown at 12 steps throughout its orbit, represented by the orange circle with an arrow denoting the axis of its rotation. The dashed line marks the major axis of Mars' orbit. Note that this diagram is not shown to scale.

### 1.2.2 Local Solar Time (LST)

While  $L_s$  marks the passage of the Martian year, time of day of a position on Phobos is represented throughout this work using Local Solar Time, or LST. Phobos is tidally locked to Mars, and so rotates at the same rate that it revolves around Mars in its orbit, taking about 7 hours and 40 minutes. However, Local Solar Time divides up each rotation into 24 “hours” of local time, so that midnight for a given location can be represented as 0000 LST, noon as 1200 LST, and so on. This allows for a simple comparison from a time of day on Phobos to the analogous time of day here on the Earth. Note that the Local Solar Time is *local*, and so dependent on both Phobos’ position in its orbit around Mars and the longitude of the surface location in question. At any given moment, all LSTs are occurring simultaneously at different longitudes around Phobos.

## 1.3 Thermal Properties and Thermal Inertia

Thermal inertia is a measure of how well a surface retains heat over time. One can observe this property directly by tracking changes in surface temperature (or by remotely tracking thermally emitted infrared radiation). Thermal inertia depends on other thermal properties, and is defined as:

$$TI = (K\rho c)^{1/2} \tag{1.1}$$

where  $K$  is the thermal conductivity,  $\rho$  is the density, and  $c$  is the specific heat of the surface material. This definition bestows thermal inertia with SI units of  $[\text{J m}^{-2} \text{K}^{-1} \text{s}^{-1/2}]$ .

For an airless regolith, like the surface of Phobos, these properties are in turn influenced by physical factors like the composition/mineralogy, particle grain size, porosity, and the abundance of larger rocks. This makes thermal inertia a convenient shorthand for comparing surface properties, and a way to infer the physical characteristics of a surface from thermal

observations. For comparison, lunar regolith, consisting of fine dust, averages around  $55 \pm 2$   $\text{J m}^{-2} \text{K}^{-1} \text{s}^{-1/2}$  (Hayne et al., 2017). Kilometer-scale Near-Earth Asteroids average  $200 \pm 40$   $\text{J m}^{-2} \text{K}^{-1} \text{s}^{-1/2}$  (Delbo' et al., 2007), corresponding to larger-scale particulates. Bare rock larger than a few tens of centimeters retains heat much longer, with a thermal inertia greater than  $\sim 1200$   $\text{J m}^{-2} \text{K}^{-1} \text{s}^{-1/2}$  (Edwards et al., 2009).

## 1.4 Goal of this Thesis

The goal of this work is to better constrain the thermal inertia of Phobos, in order to better understand the evolutionary history of Phobos and the Mars system. To that end, we have asked the following questions. We have attempted to address each of them, though some lines of inquiry have produced more conclusive results than others.

1. What is the global average thermal inertia on Phobos?
2. How does thermal inertia vary across Phobos' surface?
3. How do these constraints impact our understanding of Phobos' thermal environment?
4. What do these new constraints imply with regards to the formation of Phobos and the evolution of the Mars system?

To answer these questions, we have collected a set of thermal infrared observations of Phobos, described in Chapter 3. We compare these observed spectra with spectra produced by a thermophysical model, described in Chapter 4. In Chapter 5, we present the results of this comparison, and we discuss their implications in Chapter 6. Among those implications is a more thorough look at the thermal environment of Phobos, which comprises Section 6.4. We begin by placing our observations within the context of all infrared observations of Phobos, which are summarized in Chapter 2.

## Chapter 2

# History of Infrared Observations of Phobos

In order to contextualize the data used in this work, we begin with a brief history summarizing the available body of observations of Phobos in the infrared. Duxbury et al. (2014), and references therein, provide a summary of all spacecraft observations of Phobos through 2014, across all wavelengths and instrument types. While there have been a wide breadth of observations of Phobos covering many wavelengths, we are concerned in this work with the thermal properties of Phobos' surface. As such, we present a summary of infrared observations, which are most relevant and useful to investigating these properties.

While three missions have been launched specifically targeting Phobos (Phobos 1 and 2, and Phobos-Grunt, each by Russia), two failed before arriving at Mars, and the other, Phobos 2, failed just as it began its observations of the moon. This means that essentially all our data on Phobos comes from missions to study Mars, missions that only make infrequent encounters with the moon at significant distances.

## 2.1 Mariner 9

The earliest infrared observations of Phobos were made by the first Mars orbiting spacecraft, Mariner 9. Upon its arrival at Mars in 1971, Mariner 9 found Mars' surface shrouded in a global dust storm, providing plenty of opportunity for observations of Mars' moons.

Mariner 9's infrared radiometer sampled two channels, one centered at  $10\ \mu\text{m}$  (sensitive from  $8.1 - 12.4\ \mu\text{m}$ ) and the other at  $20\ \mu\text{m}$  ( $17.8 - 25.1\ \mu\text{m}$ ) (Chase, 1969).

13 infrared observations of Phobos were collected from a range of 5758–15,245 km, with 9 of these having Phobos well-centered in the radiometer's field of view. Even in the closest of these observations, Phobos only filled a maximum of  $\sim 20\%$  of the field of view. The instrument was tracked across Phobos, with the position verified by Mariner 9's television camera, with which the infrared radiometer was co-bore-sighted. These observations covered a range of phase angles, from  $25^\circ$  to  $85^\circ$ . In order to calibrate the absolute brightness of these observations, the instrument team referred to observations of Mars collected during Mars approach, when Mars subtended a similar solid angle. An additional set of observations was made on December 12, 1972, during and after emerging from an eclipse by Mars (Gatley et al., 1974).

Both the eclipse observations and the prior observations were compared to a simple thermal model. In each case, results were consistent with a low-conductivity surface, with Gatley et al. concluding that Phobos' surface was covered in at least 1 mm of fine dust with a conductivity  $\lesssim 4 \times 10^{-4}\ \text{W m}^{-1}\ \text{K}^{-1}$ . While the authors do not translate this to thermal inertia, we can do so using equation 1.1. Assuming a near-surface bulk density of  $1100\ \text{kg m}^{-3}$  and a heat capacity of  $0.5\ \text{J g}^{-1}\ \text{K}^{-1}$  (similar to lunar regolith (Hayne et al., 2017)), this conductivity translates to a thermal inertia of  $\sim 15\ \text{J m}^{-2}\ \text{K}^{-1}\ \text{s}^{-1/2}$ .

## 2.2 Viking

The Viking 1 and Viking 2 orbiters arrived at Mars in June and August 1976, respectively, and remained in orbit mapping the surface of Mars after deploying their landers. Viking 2 operated through July of 1978, and Viking 1 until November of 1982.

The two orbiters carried a pair of infrared radiometers, the Infrared Thermal Mappers (IRTMs). Each IRTM observed at 6 spectral channels centered at 1.5, 7, 9, 11, 15, and 20  $\mu\text{m}$ . Its 4 telescopes each fed light to 7 detectors, arranged in a chevron pattern, with each detector having a 5.2 mrad field of view (Chase et al., 1978).

The two orbiters made numerous observations of Phobos from distances greater than 1600 km, in which Phobos did not fill the field of view of any of the IRTM's 7 detectors. These covered a range of phase angles from  $\sim 0^\circ - 130^\circ$ . A further 8 close approaches provided IRTM observations from distances less than 1600 km, allowing for observations of Phobos' surface in which the IRTM field of view was fully filled. An additional series of observations were made during 8 eclipses of Phobos by Mars (Lunine et al., 1982).

Lunine et al. compared these observations to the thermal model of Kieffer et al. (1977). Their results refined those of Gatley et al. (1974), from the Mariner 9 observations, finding a generally low thermal inertia of  $\sim 40 - 70 \text{ J m}^{-2} \text{ K}^{-1} \text{ s}^{-1/2}$ .

## 2.3 Phobos 2

Phobos 2, the last interplanetary mission mounted by the Soviet Union, arrived at Mars in January of 1989, but was lost to a computer malfunction only a few days after first pointing its instruments toward Phobos, in March of the same year (Sagdeev & Zakharov, 1989). Phobos 2 carried several infrared sensing instruments.

The Combined Infrared Radiometer/Photometer (KRFM) paired a 9 band UV – visible

– near-infrared ( $0.3 - 0.9 \mu\text{m}$ ) spectrophotometer with a 6 band thermal infrared radiometer, with channels centered at  $\sim 5, 7, 8, 12, 15,$  and  $30 \mu\text{m}$ . (Ksanfomality et al., 1989). Two tracks across the surface were collected from a distance of 190 km. These observations were the subject of later analysis by Kührt et al. (1992), who used a thermal model to deduce a thermal inertia of  $20 - 40 \text{ J m}^{-2} \text{ K}^{-1} \text{ s}^{-1/2}$  and significant surface roughness.

The Infrared Spectrometer (ISM) was a near-infrared spectrometer with  $\sim 20 \text{ nm}$  resolution, ranging from  $0.8 - 3.5 \mu\text{m}$ . ISM collected two sets of Phobos observations, each from a distance of  $\sim 200 \text{ km}$ , totaling about 600 spectra (Bibring et al., 1989). Bibring et al. (1992) combined ISM and KRFM spectra to analyze Phobos’ surface composition.

A third instrument, a scanning infrared radiometer called Thermoscan, was a two channel, pushbroom style scanning thermal imager with two infrared channels centered at  $0.8$  and  $10 \mu\text{m}$ . However, no observations of Phobos were reported (Selivanov et al., 1989).

## 2.4 Mars Global Surveyor (MGS)

Mars Global Surveyor entered orbit around Mars in September of 1997. It encountered Phobos 4 times between August and September of 1998, during its Science Phasing Orbits (Albee et al., 2001). The Thermal Emission Spectrometer (TES) instrument (Christensen et al., 2001) collected several hundred infrared spectra of Phobos’ surface during these close approaches, including those used in this work. Section 3.2 discusses the observations collected on these encounters in more detail. Section 3.3 discusses the TES instrument.

## 2.5 Ground-based observations

With time, technological advancements created the opportunity to observe Phobos in the infrared from Earth-based telescopes. Rivkin et al. (2002) and Lynch et al. (2007) each

observed Phobos with NASA’s 3 meter Infrared Telescope Facility (IRTF) on Mauna Kea, Hawaii.

Rivkin et al. performed spectrophotometry of both the “red” and “blue” spectral units identified by Murchie & Erard (1996). The instruments used in this study were NSFCAM, a near-infrared imaging array, using a circular variable filter at 11 wavelengths between 1.65 – 3.50  $\mu\text{m}$ , in conjunction with the Cold Coronagraph (CoCo), used to observe faint sources in close proximity to bright ones (a critical challenge when observing the moons of Mars from Earth) (Shure et al., 1994; Wang et al., 1994; Toomey et al., 1998). The spectra collected were corrected for their thermal component by applying the thermophysical model of Lebofsky & Spencer (1989), using the thermal inertia derived from Phobos 2 measurements by Ksanfomality et al. (1991); however, as the focus of Rivkin et al.’s work was Phobos’ spectral features, no independent analysis was performed regarding its thermal properties.

Lynch et al. (2007) report 3 – 13  $\mu\text{m}$  spectra of Phobos collected using IRTF’s Broadband Array Spectrograph System (BASS) (Hackwell et al., 1990). Lynch et al. compared their results with a Standard Thermal Model, but were unable to produce reasonable fits to their spectra that could adequately match the behavior at both short (4 – 5  $\mu\text{m}$ ) and longer (8 – 13  $\mu\text{m}$ ) wavelengths. The authors suggested emissivity variability across the observed wavelengths as a possible solution. They also noted that the observed brightness temperature exceeded that predicted by their model, pointing to thermophysical modeling (specifically, that of Giese & Kührt (1990)) as an improved approach.

## 2.6 2001 Mars Odyssey (Odyssey)

Mars Odyssey arrived at Mars October 24, 2001, but it was not until September 29, 2017, that it would observe Phobos with its THEMIS instrument (Bandfield et al., 2018). The Thermal Emission Imaging System (THEMIS) is a multispectral imager with 5 visible/near-

infrared bands between  $0.42 - 0.86 \mu\text{m}$  and 9 thermal-infrared bands from  $6.8 - 14.9 \mu\text{m}$ . It was intended to link the global hyperspectral map of Mars produced by TES to smaller spatial scale features, with 100 m per pixel resolution from Odyssey’s primary mapping orbit. Its uncooled microbolometer detector array contains  $320 \times 240$  pixels, each with an instantaneous field of view of  $\sim 0.25$  mrad, for a total field of view of  $80 \times 60$  mrad ( $4.6^\circ \times 3.5^\circ$ ). The co-boresighted visible imager provides higher-resolution context images with an array of  $1024 \times 1024$  pixels and a tighter field of view ( $46.4 \times 46.1$  mrad, or  $2.66^\circ \times 2.64^\circ$ ) (Christensen et al., 2004).

Bandfield et al. (2018) report their first set of observations using THEMIS, but have continued to collect further observations as favorable encounters between Phobos and Odyssey occur. Their first observations, collected from a range of  $\sim 5500$  km, achieved a spatial resolution of 1.3 km per pixel. As Odyssey is in its low, mapping orbit around Mars, this represents nearly the best possible resolution available to THEMIS. The September 2017 observations covered the morning hemisphere of Phobos, spanning a range of local solar times (LST) from 0600 LST to 1030 LST. Observations were somewhat consistent with thermal modeling performed assuming a thermal inertia of  $\sim 150 \text{ J m}^{-2} \text{ K}^{-1} \text{ s}^{-1/2}$ , though a more successful model varied thermal inertia with depth, from  $50 - 1000 \text{ J m}^{-2} \text{ K}^{-1} \text{ s}^{-1/2}$ , with an h-parameter<sup>1</sup> of 0.04 m, after similar modeling performed for lunar regolith (Hayne et al., 2017).

## 2.7 Mars Reconnaissance Orbiter (MRO)

Mars Reconnaissance Orbiter entered Mars orbit on March 10, 2006. On October 23, 2007, about a year into its primary mapping phase, MRO turned its instruments toward Phobos. The Compact Reconnaissance Imaging Spectrometer (CRISM) is a hyperspectral

---

<sup>1</sup>a parameter controlling the rate of change in thermal inertia with depth, with density at depth scaling with  $e^{-h}$

visible/near-infrared imager, covering  $0.362 - 3.920 \mu\text{m}$  with 544 channels, achieving a spectral resolution of  $6.55 \text{ nm/channel}$ , and a spatial resolution of  $60 \mu\text{rad/pixel}$  (Murchie et al., 2007). CRISM collected three images of Phobos, with 350 m per pixel spatial resolution, at a phase angle of  $\sim 41^\circ$ . These generally captured the western portion of the sub-mars hemisphere (Murchie et al., 2008).

Fraeman et al. (2012) analyzed these images, applying the thermal model of Kuzmin & Zabalueva (2003) to remove the thermal component of their spectra. Fraeman et al. (2014) performed further analysis using these data to constrain Phobos' surface mineralogy, detecting neither olivine nor pyroxene in either spectral unit. These near-infrared observations could not be used to determine thermal properties.

## 2.8 Mars Express (MEx)

Mars Express reached Mars on December 25, 2003. Due to its polar and eccentric orbit, Mars Express has the best circumstances of any spacecraft currently operating at Mars to observe Phobos up close, including several approaches closer than 100 km. As of 2014, the Planetary Fourier Spectrometer (PFS) had made observations of Phobos on 42 orbits, and the OMEGA imaging spectrometer had observed Phobos on 30 orbits (Witasse et al., 2014).

OMEGA, the Observatoire pour la Minéralogie, l'Eau, les Glaces et l'Activité, is a visible/near-infrared imaging spectrometer with a visible channel operating between  $0.38 - 1.05 \mu\text{m}$ , and a near-infrared channel operating between  $0.93 - 5.1 \mu\text{m}$ . (Bibring et al., 2004). OMEGA observation of Phobos comprised a large portion of the Fraeman et al. (2012) and Fraeman et al. (2014) compositional analyses, previously mentioned above in section 2.7.

PFS is a double pendulum interferometer, with a short wavelength channel between  $1.2 - 5.7 \mu\text{m}$  and a field of view of  $1.6^\circ$ , and a long wavelength channel between  $5.5 - 45 \mu\text{m}$  and a

field of view of  $2.8^\circ$ . Both channels are sampled evenly in wavenumber space with a  $1.3 \text{ cm}^{-1}$  spectral resolution, or  $\sim 1100$  distinct channels in the long wavelength range. (Formisano et al., 2005)

Giuranna et al. (2011) applied PFS spectra of Phobos, along with spectra collected by TES, to analyze Phobos' surface composition, with results consistent with the presence of silicates in both the red and blue spectral units. The authors also derived surface temperatures from each instrument's observations. These temperatures were then compared to the model of Kuzmin & Zabalueva (2003), generally agreeing with those predictions. However, neither the temperature measurements collected by TES nor those of PFS were used to independently derive the thermal inertia of the surface.

## 2.9 Future Missions

With the failure of Roscosmos' Phobos-Grunt mission shortly after its launch in 2011, the prospect for a dedicated mission to Phobos was cut short. Numerous proposals were drafted and evaluated within space agencies around the world. One, so far, has seen success and is in active development. The Japanese space agency, JAXA, plans to launch its Mars Moons Exploration (MMX) mission in 2024. Its payload includes a near-infrared imaging spectrometer, MacrOmega, with a wavelength range of  $0.9 - 3.6 \mu\text{m}$  (Iwata et al., 2017). While this instrument will provide valuable global near-infrared hyperspectral mapping, it will not be suited to identifying small-scale spatial variability in Phobos' thermophysical properties. The MMX mission will land on Phobos' surface, however, and carry a sample of its regolith back to Earth for analysis. Such a sample will provide critical "ground-truth" regarding the physical characteristics of Phobos' regolith. Assuming a successful mission, Phobos samples will be returned to Earth by 2029.

Table 2.1 Summary of Estimates of Phobos’ Thermal Inertia

Mission	Thermal Inertia ( $\text{J m}^{-2} \text{K}^{-1} \text{s}^{-1/2}$ )	Reference
Mariner 9	$\lesssim 15$	Gatley et al. (1974)
Viking	$\sim 40 - 70$	Lunine et al. (1982)
Phobos 2	$\sim 20 - 40$	Kührt et al. (1992)
Mars Odyssey	$\sim 150^*$	Bandfield et al. (2018)

---

Note. — Mars Odyssey results preliminary. The authors also suggest a depth-dependent thermal inertia varying from 50 – 1000  $\text{J m}^{-2} \text{K}^{-1} \text{s}^{-1/2}$ .

## 2.10 Summary of Estimates of Thermal Properties

Between these numerous missions, infrared instruments, and authors, only 4 independent estimates of Phobos’ surface thermal properties have been made, summarized in Table 2.1.

In addition to the observations by Mars Global Surveyor which are the subject of this work, an additional set of observations has not been used to derive thermal properties, which may yet yield an an independent estimate of thermal inertia. The PFS observations from the Mars Express spacecraft cover the appropriate wavelength range, with adequate spectral resolution. This dataset provides a ripe opportunity for future work applying the methodology used here to cover a wider range of local times and solar longitudes.

# Chapter 3

## Observations

### 3.1 Choice of Dataset

The observations used in this work were collected by the Thermal Emission Spectrometer (TES) instrument carried on Mars Global Surveyor. This dataset has not previously been applied to the question of Phobos' thermophysical properties. TES's observations of Phobos are well-suited among the collection of infrared observations to this task.

1. TES spectra spanned a broad wavelength range, covering the regime dominated by thermal emission. Observations by near-infrared instruments (e.g., Phobos 2's ISM (Section 2.3), MRO's CRISM (Section 2.7), MEx's OMEGA (Section 2.8)) are dominated by reflected sunlight, and cannot be used to determine thermal properties.
2. TES had high spectral resolution, with 143 channels at  $10 \text{ cm}^{-1}$  intervals. This is in contrast to lower spectral resolution observations by Odyssey's THEMIS (Section 2.6), Phobos 2's KRFM (Section 2.3), Viking's IRTM (Section 2.2), and Mariner 9's IR Radiometer (Section 2.1).
3. TES observations covered a wide range of local times, directly revealing the effects of

thermal inertia by measuring temperature changes over time.

4. TES's spatial resolution, though surpassed by later instruments, was the highest ever for a thermal IR instrument at the time these observations were collected.

## 3.2 Mars Global Surveyor Encounters with Phobos

Mars Global Surveyor (MGS) launched on November 7, 1996 (Albee et al., 2001). Its primary mission was to produce a global map of Mars using its suite of various instruments: MOLA, a laser altimeter; MOC, a visible-light camera; TES, an infrared spectrometer; a magnetometer; and a radio science package. By necessity, MGS' main science orbit was required to be polar, so as to achieve coverage at all latitudes; circular, to have consistent spatial resolution; and sun-synchronous (that is, to pass over the same local solar times (LST) on each orbit). The target orbit would travel north to south over the 14:00 LST longitude on Mars' surface, then return from south to north over the night side at the 02:00 LST longitude. To remain in this position, the orbit would precess at the same rate that Mars orbited the Sun; for each degree Mars traveled in its orbit, MGS's orbit would likewise precess around Mars. This orientation would be ideal for mapping, as it kept the sun high overhead and with a consistent shadow direction across all observations (Albee et al., 1998).

MGS achieved Mars Orbital Insertion on September 11, 1997 on an elliptical orbit with a 44.993 hour period and an inclination of  $93.258^\circ$  (Albee et al., 2001). To circularize and lower this initial capture orbit, the mission design called for a series of aerobraking maneuvers over a period of around four months. This involved dipping the spacecraft into the thin upper Martian atmosphere just enough that drag would reduce its velocity, decreasing its apoapsis altitude and period.

Aerobraking had been experimentally demonstrated in 1991 in Earth's atmosphere during the Japanese Hiten mission to the Moon, and had been applied in 1993 during the extended

mission of Magellan at Venus (Lyons et al., 1995). However, this would be the first time aerobraking was used as a critical aspect of a spacecraft’s primary mission, and the first time in the atmosphere of Mars. Aerobraking added complexity and risk to the mission design, but provided an opportunity to circularize MGS’s orbit without expending any propellant. Every kilogram of propellant saved represented many kilograms saved in launch mass, and the savings allowed the use of a smaller Delta II launch vehicle, so the trade-off was deemed advantageous. Aerobraking has continued to be used successfully at Mars and throughout the solar system, including by NASA’s Mars Odyssey and Mars Reconnaissance Orbiters, as well as ESA’s ExoMars Trace Gas Orbiter.

One month into the planned aerobraking period, damage to one of MGS’s two solar panels was discovered, halting the aerobraking while the fault was investigated. The damage stemmed from the fracture of a damper arm during the initial deployment of the solar panels on departure from Earth.<sup>1</sup> As presented by Albee et al. (1998), the damaged panel could not safely bear the drag pressure endured during each pass through the atmosphere. To reduce this pressure, mission planners designed a less aggressive campaign of aerobraking, maintaining a higher altitude in the atmosphere than initially planned. The new plan attenuated the dynamic pressure on the solar panels to a third of that of the original plan, from 0.68 – 0.58 N m<sup>2</sup> to 0.25 – 0.15 N m<sup>2</sup> (Albee et al., 2001).

The new aerobraking campaign spread the stresses to MGS over a longer period, but this meant the spacecraft would miss its opportunity to arrive in its intended sun-synchronous orbit. In order to preserve the sun angle for which all of MGS’s instruments had been designed, an additional delay was required, during which no aerobraking was performed. This delay, a phase termed Science Phasing Orbits in the mission chronology, was timed to coincide with the interruption of operations due to the conjunction of Mars with the Sun.

---

<sup>1</sup>I note for the reader that perhaps without the failure of a damper arm nearly 22 years ago, this thesis would not exist.

Aerobraking was performed in two phases, with the Science Phasing Orbits in between. The total duration of these activities took half of one Martian year, with MGS arriving in its mapping orbit February 19, 1999, 17 months after Mars Orbital Insertion. This half-Mars-year delay placed MGS not in its target 14:00 – 02:00 LST sun-synchronous orbit, but its 180° reflection, traveling south to north along the 14:00 LST longitude, and north-south along the 02:00 LST longitude. Though its direction of travel was reversed, this orbit allowed MGS to maintain the Mars surface illumination conditions over which MGS’s instruments had been designed to operate (Albee et al., 2001).

Throughout the Science Phasing Orbits, observations of Mars’ surface were made using MGS’ suite of instruments. It was during this period of the mission that MGS’s orbit made several close approaches to Phobos. This afforded the opportunity for MGS to observe Phobos before beginning its main scientific mission.<sup>2</sup>

Mars Global Surveyor encountered Phobos four times, between August 7 and September 12, 1998. Each encounter, logically, occurred at the intersection of MGS’s orbit and that of Phobos. Figure 3.1 shows the orbits of MGS and Phobos during each of the four encounters, and Table 3.1 lists relevant information for the observations made during each close approach. Due to MGS’ near-polar orbital inclination, and Phobos’ near-equatorial inclination, this intersection occurred at only one location in the two objects’ respective orbits, relative to the Mars-centered inertial reference frame.<sup>3</sup> As the four encounters occurred over a span of only a few weeks, the angle formed by the Sun, Mars, and Phobos at the time of each close approach changed very little,  $\sim 15^\circ$ , as seen in the last column of Table 3.1. Section 3.5 discusses the implications of this for the illumination conditions observed in our data set.

During these close approaches, the Thermal Emission Spectrometer (TES) instrument

---

<sup>2</sup>Mission status reports at the time are less interested in the potential scientific value of these close approaches, celebrating that MGS “avoided a collision with the Martian moon Phobos as it crossed its orbital path three times.” (Johnston et al., 1999)

<sup>3</sup>MGS’ orbit did precess slightly over the span of these encounters, but the effect this had on the observed illumination of Phobos was small compared to other influences.

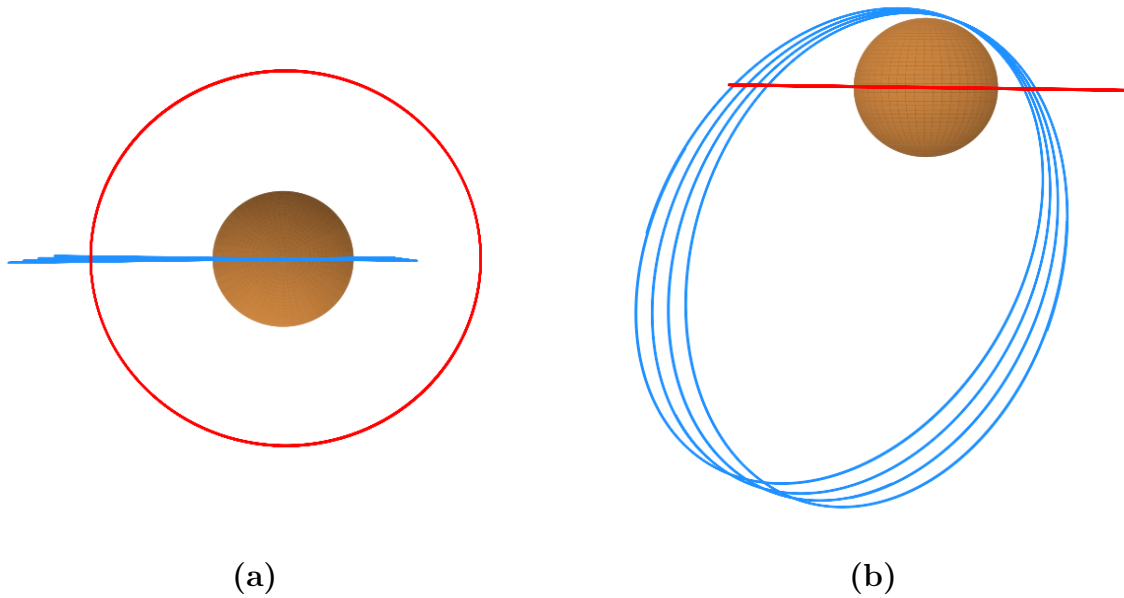


Figure 3.1 Views of the orbits of Phobos (red) and MGS (blue) from above Mars' north pole **(a)**, and above Mars' equator, perpendicular to the orbital plane of MGS **(b)**. The MGS orbits shown are the four orbits on which MGS encountered Phobos, as described in Table 3.1. Orbits are plotted relative to the Mars-centered inertial reference frame oriented with Mars' North pole along the  $+\hat{Z}$  axis. Note that each MGS encounter with Phobos occurred at nearly the same location in Phobos' orbit, explaining the consistent illumination conditions across the three sets of observations. In the left view, sunlight arrives from the bottom of the figure, and on the right, from the direction of the viewer.

Table 3.1 Summary of Observations Used in This Work

OCK	# of Obs.	Mars $L_s$	UTC Date	Timespan of Obs.	S-M-P Angle
476	0	11.66	1998 Aug 7	—	83.3°
501	7	17.45	1998 Aug 19	14s	87.4°
526	24	23.15	1998 Aug 31	5m 10s	91.4°
551	325	28.76	1998 Sep 12	5m 2s	98.6°

Note. — S-M-P Angle is the angle made by the Sun, Mars, and Phobos at the time of observation. As discussed in Section 3.5, the S-M-P Angle varies only slightly between our observations, meaning across all our observations, the LST of a given location only varies by  $\sim 3\%$ . As detailed in Section 3.4, only observations in which Phobos filled the detector field of view were used in this work. As such, no observations were used from OCK 476.

collected mid-infrared spectra of Phobos’ surface. As detailed in Section 3.3, TES is a mid-infrared interference spectrometer operating between  $\sim 150 - 1700 \text{ cm}^{-1}$  ( $\sim 6 - 67 \mu\text{m}$ ), designed to globally map the mineralogy of Mars. Each of its six detectors have an instantaneous field of view of  $\sim 8 \text{ mrad}$  ( $\sim 0.5^\circ$ ). Under the Orbit Counter Keeper (OCK) numbering system used by the TES instrument team, the Phobos encounters occurred during OCKs 476, 501, 526, and 551. In each case, the spectra used in this work were collected over the span of approximately 5 minutes or less. A summary of our observations is given in Table 3.1.

### 3.3 Thermal Emission Spectrometer (TES)

We have assembled a set of mid-infrared spectra collected by Mars Global Surveyors Thermal Emission Spectrometer (TES) (Christensen et al., 2001). TES is a Fourier transform Michelson interferometer, co-aligned with two bolometers: a thermal bolometer with a  $5 - 100 \mu\text{m}$  bandpass, and a visible bolometer with a  $0.3 - 3 \mu\text{m}$  bandpass. The interferometer’s 6 infrared pyroelectric detectors are arranged in a  $2 \times 3$  array, each with an instantaneous field of view of  $\sim 8 \text{ mrad}$  ( $\sim 0.5^\circ$ ), and a 1.8 s integration time. Light is collected via a

rotating pointing mirror, which, during Mars-oriented operations, allows for observation of empty space, the Martian limb, any position along MGS' ground track, as well as an internal calibration source. This pointing mirror allows TES to be pointed along a single axis<sup>4</sup>, independently from MGS' orientation, rather than being a static, nadir-pointed instrument.

Each spectrum consists of 143 channels, ranging from  $\sim 150 - 1700 \text{ cm}^{-1}$  ( $\sim 6 - 67 \text{ }\mu\text{m}$ ) and sampled in wavenumber space at  $\sim 10 \text{ cm}^{-1}$  intervals. For this work, we are primarily concerned with surface thermal properties, rather than composition. As such, rather than work directly with the radiance reported by TES for each channel, we used the brightness temperature corresponding to these measurements. The brightness temperature was determined by using the Planck function to convert (non-emissivity corrected) radiance to temperature (Christensen et al., 2001). We expect that using the non-emissivity corrected radiance introduces only a very small uncertainty into our observations.

As TES was designed to achieve high spectral resolution, it has been used extensively to identify and interpret compositional features across the surface of Mars. Smith et al. (2000) demonstrated a method to remove the influence of the Martian atmosphere in spectra of Mars' surface. Hamilton et al. (2003) used TES to search for potential source regions for Martian meteorites. Giuranna et al. (2011) used these Phobos observations, as well as observations from the Planetary Fourier Spectrometer on the Mars Express spacecraft, to interpret Phobos' surface composition.

TES spectra are also applied to derive thermal properties across Mars. Mellon et al. (2000) found good agreement between Mars surface thermal inertias derived from TES spectroscopic brightness temperatures and  $5.5 \text{ }\mu\text{m} - 100 \text{ }\mu\text{m}$  bolometric brightness temperatures. Putzig (2006) used TES's global coverage to derive a complete map of Mars' thermal inertia (which ranges from less than  $40$  to greater than  $700 \text{ J m}^{-2} \text{ K}^{-1} \text{ s}^{-1/2}$ ) at a resolution of  $0.05^\circ$  ( $\sim 3 \text{ km}$ ).

---

<sup>4</sup>In Mars observations, this gave TES an additional degree of freedom along MGS' ground track.

## 3.4 Selection of Observations

For each of our selected measurements, the field of view of the detector collecting the spectrum wholly intersected the surface of Phobos, i.e., Phobos wholly filled the field of view. This was done as a way to simplify our dataset by ignoring cases where any portion of the field of view was occupied by empty space.

In order to determine which TES observations fit this criterion, NAIF’s SPICE software was used to determine the intersection of the TES field of view with the surface of Phobos. Each observation’s footprint was mapped to the Phobos surface by casting rays from the relevant detector, positioned within SPICE according to the spacecraft clock time of that observation. 400 rays were cast for each observation, arranged in a  $20 \times 20$  grid, representing  $\sim 0.4$  mrad angular increments across each detector instantaneous field of view. Each ray was then intersected with the Phobos triaxial ellipsoid, positioned according to the given spacecraft clock time. The time between the start and end of the acquisition of each spectrum (1.8 seconds) was accounted for in the footprint determination to ensure any spacecraft motion would be accurately translated to the surface. The latitude and longitude of each intersection—along with other ancillary parameters (such as local time)—were recorded, generating up to 400 grid points on Phobos’ surface.

The boundary surrounding each detector’s grouping of points was found using a convex hull method. The number of points defining this polygonal boundary was reduced to the minimum necessary to account for deviations. Observations where all 400 grid points intersected the Phobos surface were considered “fully filled”. Accurate polygons were created for all footprints, regardless of if they were “fully filled” or not. However, observations not filling the field of view were not used as a part of this study, due to the complexities of modeling high emission angles along the limb and mixtures of temperatures between space and Phobos. These non-filled observations, including all observations from OCK 476, were

discarded.

The field of view perimeter for each observation formed an irregular polygon based on the inclined angle of the observation and Phobos' irregular surface. While previous authors have performed analyses of TES observations of Phobos with approximate field of view footprint positions (e.g., Giuranna et al. (2011)), this is the first mapping of TES observations to polygonal surface regions on Phobos.

The thermal model used in this work, described in Chapter 4, decomposes the surface of Phobos into triangular facets. In order to convert our latitude-longitude polygon into a usable format for the thermal model, we identified the set of facets in the Gaskell (2011) Phobos shape model that corresponded to the polygonal surface region. Once identified, this collection of facets was then passed to the thermal model to model each observation, as described in Chapter 4.

The set of facets is combined with three vectors describing the positions of Mars, the Sun, and MGS, relative to Phobos, at the time of the observation. This provides the model with all the necessary geometric information to model the temperature of each facet, and subsequently determine the radiance contribution from each part of the observed region as viewed by TES.<sup>5</sup>

### 3.5 Summary of Observations

The 356 observations covered a total of 58.5% of the surface of Phobos. 48.5% of the surface was observed more than once, with a handful of facets (540, or 1.1%) being observed 40 or more times.

---

<sup>5</sup>The relative contribution of each facet to the overall observation depends on both the overall emission from that facet and the solid angle it subtends. A hotter facet will radiate more strongly than a cooler facet. A facet which is highly inclined to the observer (i.e., a portion of Phobos highly inclined to TES) contributes very little to the total radiance detected, whereas a facet of equal physical area which is oriented orthogonal to the observer's line of sight will have a much greater contribution.

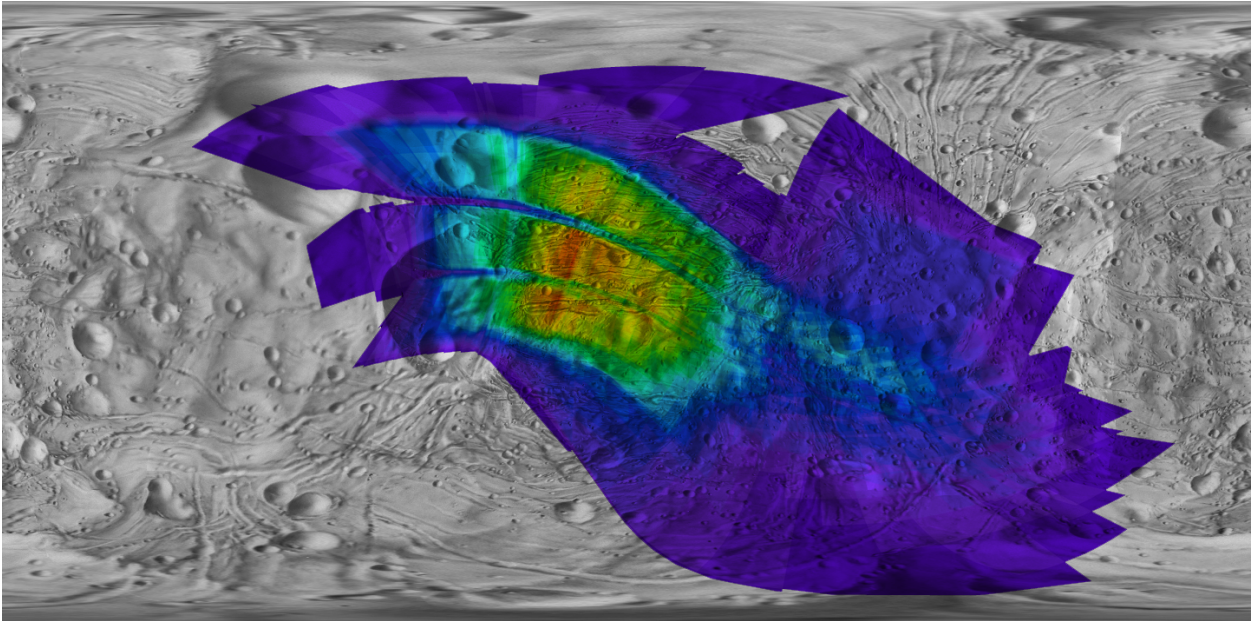


Figure 3.2 Map of Phobos, showing the extent of coverage by our collection of observations. Color shows the number of observations of a given location, ranging from 1 (purple) to 49 (red). Given the illumination conditions during our observations, this map is roughly centered on the evening terminator.

As shown in table 3.1, our observations are drawn from MGS’s encounters with Phobos during OCKs 501, 526, and 551. No observations during OCK 476 satisfied our requirement that the detector field of view be fully filled by Phobos. These three encounters fell just after Mars’ northern Spring equinox, at  $L_s = 17.45, 23.15,$  and  $28.76$ . For Phobos, this means at the time of these observations, the heliocentric distance was  $\sim 1.6$  AU, close to its mean value of 1.53 AU.

These observations covered a range of local times, with local time at the center of included facets ranging from  $\sim 12:00$  LST through midnight to  $\sim 04:00$  LST. 180 observations were entirely illuminated by sunlight, 80 fell along the evening terminator (partly illuminated, partly shadowed), and 96 were entirely in shadow. A selection of several observations, demonstrating the range in footprint size and local time, is shown in figure 3.3. As will be addressed further in section 6.2, observations centered over the terminator present a unique

challenge to model. If an observation footprint straddles the terminator, it will contain some regions that are illuminated, and some that are not. The surface temperature will vary greatly across the observed region, with each spectrum being the combination of emission at a mixture of temperatures.

Over the  $\sim 3.5$  weeks spanned by our observations, Mars traveled a few degrees ( $\sim 11$ ) forward in its orbit around the Sun. This changed the angle formed by the Sun, Mars, and Phobos at the time of each encounter, but only by a small amount ( $11.2^\circ$ ). As Phobos rotates synchronously with its orbit, this means that during each encounter between MGS and Phobos, Phobos was under quite similar illumination conditions, with the same hemisphere facing the Sun. Thus, despite making observations during three separate encounters, each observation of a given surface location was always made at roughly the same local time (varying by  $\sim 3\%$ ).

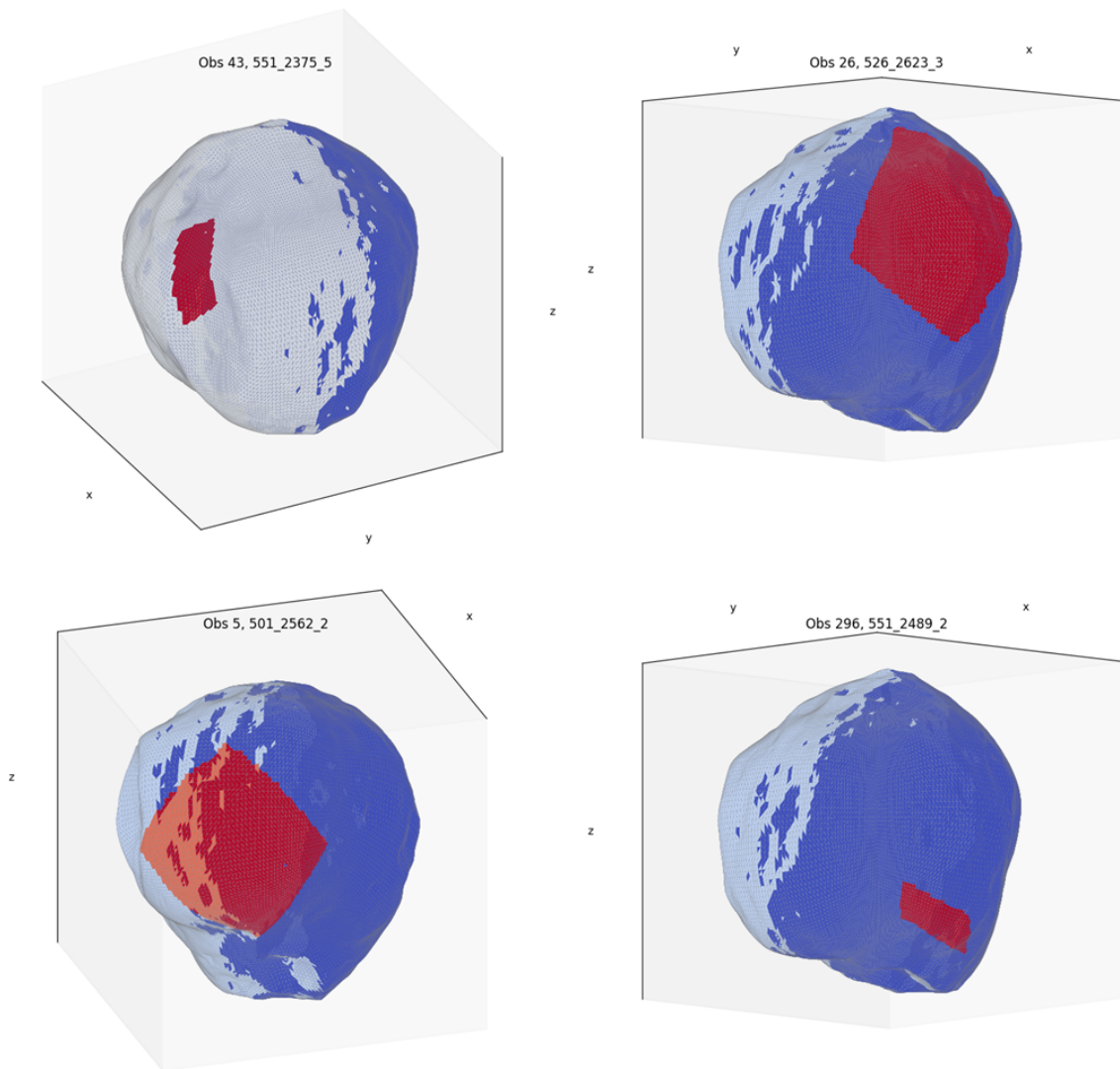


Figure 3.3 Views of Phobos, showing individual TES observation footprints (highlighted in red, against blue un-observed regions), and solar illumination. Illuminated surface facets are lighter in color, and un-illuminated facets are darker. The selected observations demonstrate the range of footprint sizes and solar times. These views also demonstrate that despite our observations being collected across three separate MGS orbits, the solar illumination conditions at Phobos remained quite similar. In each view, the evening terminator falls near  $0^\circ$  longitude (the Mars-facing hemisphere). Clockwise from upper left, these observations were collected in OCKs 551, 526, 551, and 501.

# Chapter 4

## Model

Our model, PhobosTPM, is a modified version of a near Earth asteroid thermophysical model called Convex, so named for its restriction to the modeling of convex bodies with no self-illumination or self-shadowing. This makes Convex a “one-dimensional model,” as heat energy is thermally transmitted only along one dimension, i.e., depth into the surface, with no communication between facets.

Convex was developed by Michael Mommert, and was used to constrain the physical properties of several near-Earth objects (NEOs) (Mommert et al., 2014a,b). This in turn built on the work of Michael Mueller, who developed a well-tested TPM in C++ (Mueller, 2007), ultimately based on Spencer (1990) and Lagerros (1996a,b, 1997, 1998).

### 4.1 Model Description

This section provides an overview of the internal processes by which our model, and its progenitor, Convex, operates. A far more thorough analytical description of both the model’s code and underlying physics was made by Mueller (2007), in addition to a comparison with other airless body thermal models, such as the STM and NEATM. The treatment offered

here is intended to familiarize the reader with the general approach taken.

### 4.1.1 Illumination of facets

When the model is first instantiated, the list of facets being modeled (i.e., those within an observation’s footprint) is read in from the appropriate file. The 49,152-facet Gaskell (2011) Phobos shape model (see Section 4.2.3) is consulted to construct each of these facets. The facets are positioned relative to the center of Phobos according to the shape model, and these Phobos-centered coordinates form the basis for the placement of illumination sources as well as the observer. The outward-pointing surface normal vector and surface area are then calculated for each facet.

The vectors describing the position of the Sun and Mars are next read from the configuration file. Using the rotational period (a parameter held constant at 7.65385 hours) and a system of coordinate transformations, these positions are then converted to a functional representation of the illumination geometry in the Phobos-centered co-rotating frame. Because Phobos’ rotation is synchronous with its orbital period, Mars remains in a fixed position in this co-rotating frame. As Phobos’ orbit is both highly circular ( $e = 0.015$ ) and highly equatorial ( $i = 1.1^\circ$ ), the small effect of Mars’ libration is not accounted for. Furthermore, as shown in Table 3.1, the observations made on each Phobos encounter spanned only a few minutes at most. The illumination conditions did not change significantly over this time period, and were assumed to be constant when modeling our observations.

The model assumes no shadowing of facets by their neighbors, so the incident flux on each facet from each illumination source is simply a function of the angle between that facet’s surface normal vector and the vector pointing to that source. That is, the incident solar flux at a facet is the solar irradiance at Mars multiplied by the cosine of the Sun’s zenith angle. The same is true for incident flux due to Mars-shine, though rather than a constant,

the cosine of Mars' zenith angle is multiplied by the result of a function defining Mars-shine for any given point in Phobos' orbit. The Mars-shine function is described in Section 4.2.2, and in greater detail in Appendix A. While no self-shadowing is accounted for in our model, eclipses of the Sun, in which Mars blocks sunlight from reaching Phobos, are taken into account, as described in Section 4.2.1.

### 4.1.2 Thermal Diffusion

The incident flux is fed to a routine that solves the heat diffusion equation in one dimension between the surface and subsurface layers. Thermal conduction can only transmit energy a few centimeters at most through Phobos' surface, compared to the typical scale of a facet of more than 100 m. Therefore we can safely ignore conduction between facets, and use a one-dimensional method to model heat diffusion.

In this case, the heat flux,  $\vec{\Phi}$ , in units of  $[\text{J m}^{-2}]$ , is inversely proportional to the gradient of temperature,  $\vec{\nabla}T$ :

$$\vec{\Phi} = -\kappa\vec{\nabla}T \quad (4.1)$$

where  $\kappa$  is the conductivity of the material, and is assumed to be constant with both temperature and depth. The heat energy per unit volume,  $\rho cT$ , is the product of the temperature  $T$ , density  $\rho$ , and specific heat  $c$ . Changes to this heat create a heat flux, transforming equation 4.1:

$$\frac{\partial}{\partial t}\rho cT = \vec{\nabla} \cdot \kappa\vec{\nabla}T \quad (4.2)$$

which reduces to the heat diffusion equation:

$$\frac{\partial}{\partial t}T = \frac{\kappa}{\rho c}\vec{\nabla}^2T \quad (4.3)$$

Our model solves Equation 4.3 numerically, using discrete subsurface layers.

The number of subsurface layers used was configurable, as was their total depth. Depth in our model was treated in units of diurnal thermal skin depths, defined as the depth at which the amplitude of the thermal heat wave diminishes by a factor of  $1/e$ . Skin depth,  $D$ , is calculated from thermophysical properties as:

$$D = \sqrt{\frac{\kappa P}{\pi \rho c}} \quad (4.4)$$

where  $P$  is the period of the cycle in question (7.65385 hours for Phobos' diurnal skin depth). Throughout our investigation, the parameters controlling the subsurface layers were held constant, with 32 layers reaching a total depth of 8 skin depths. Treating depth in units of skin depths rather than physical units means the model can solve the heat diffusion equation without directly knowing the individual thermal properties of the surface. However, using appropriate estimates for the relevant thermal properties, we can estimate the diurnal skin depth to be on the order of  $\sim 7$  mm, giving us a total modeled depth of about 5 cm.

To find solutions to Equation 4.3, we require two boundary conditions. At infinite depth, the change in temperature approaches 0. At the surface, the thermal emission of heat into space (according to the Stefan-Boltzmann law) is balanced by the absorption of heat from all illumination sources (i.e., the Sun and Mars) plus conduction from the subsurface:

$$\epsilon \sigma T^4 = (1 - A)I_S \cos \theta_S + (1 - A)I_M \cos \theta_M + \Phi \quad (4.5)$$

where  $\epsilon$  is the emissivity,  $\sigma$  is the Stefan-Boltzmann constant,  $A$  is the albedo,  $I_S$  and  $I_M$  are the irradiance from the Sun<sup>1</sup> and Mars<sup>2</sup>, respectively,  $\theta_S$  and  $\theta_M$  are the zenith angles of the Sun and Mars, respectively, and  $\Phi$  is the upward heat flux from the subsurface (Mueller,

---

<sup>1</sup>Solar irradiance is calculated by dividing the Solar constant at 1 AU ( $S_0 = 1360$  W/m<sup>2</sup>) by the distance,  $r$ , from the Sun, squared ( $I_S = S_0/r^2$ ).

<sup>2</sup>Irradiance from Mars, or Mars-Shine, varies along Phobos' orbit. It is defined in the model by a function, as described in brief in section 4.2.2, and in greater detail in Appendix A.

2007, § 3.2.2).

The albedo of each facet could be varied independently, but a constant albedo of 0.07 was assumed throughout all of our trials (Kuzmin & Zabalueva, 2003). We hope to refine our model in the future using a global albedo map, should one become available. Absorption of solar radiation depends on a factor of  $(1 - A)$ , so small refinements in albedo will not produce strong influences on our results.

### 4.1.3 Surface Roughness

Surface roughness is accounted for by adding hemispherical craters to the surface of each facet. Within a crater, radiation that is scattered or emitted has some chance of being reabsorbed at some other location in the crater. This process may occur multiple times, with light being scattered and emitted multiple times before its energy is either absorbed into the subsurface or emitted back to space. When the Sun is high over the facet, this leads to increased absorption of incident light, effectively lowering albedo and increasing surface temperature. When the Sun is low over a facet's horizon, shadowing reduces the portion of the surface absorbing energy, while the area emitting energy remains the same, lowering apparent temperatures (Mueller, 2007, § 3.2.3).

In a natural surface, below the scale of individual facets, roughness takes a variety of shapes, sizes, and forms, with an irregular, fractal-like nature. Modeling sub-facet scale roughness as hemispherical craters, which are in turn comprised of triangular sub-facets, does a good job of approximating this effect, as modeled craters can be thought of as independent of size on an essentially infinite facet (Lagerros, 1998). The strength of this effect is controlled by two parameters within the model:

1. The crater opening angle determines essentially how deeply the crater excavates the planar facet surface, with a small value creating a shallow depression, and the maximum

Table 4.1 Summary of Surface Roughness Conditions

Opening Angle	Crater Density
0.0°	0.0
117.7°	0.4
144.6°	0.6
151.8°	1.0

of 180° creating a full hemisphere.

2. The crater density determines the fraction of the surface that is “cratered,” and that which remains planar.

We examined 4 roughness conditions, summarized in Table 4.1, corresponding to the zero, low, medium, and high roughness values examined by Müller et al. (2004).

#### 4.1.4 Solving for Surface Temperature

Taking all of the above factors into account, the one-dimensional heat diffusion equation is solved, and a surface temperature is found for each facet.

This process is then repeated for each time step in Phobos’ rotation. The number of time steps per rotation was configurable as a logistical parameter. In all our trials, we divided each rotation (i.e., each orbit) into 800 steps.

The model advances time, step by step, until it returns to its initial rotation state. Each time it returns to this initial state, it calculates the difference in surface temperature between the temperature on the current rotation, and the temperature found on the previous rotation. over many iterations, the model should converge on a result, and the temperature difference from one orbit to the next should become small. Once this temperature difference is within a specified accuracy requirement, the model halts, and records the final surface temperature of that facet. The required accuracy is configurable, and throughout our investigations was set at 1 part in 10,000.

### 4.1.5 Calculation of Observed Flux

Once the surface temperature is found for each facet, the observer location is determined from the configuration file, and the observed flux from each facet is calculated for each wavelength of interest. Finding a facet's observed flux  $F$  involves combining the contributions of directly emitted flux  $F_0$  and all orders of scattered flux  $F_i$  originating from surface roughness subfacets  $dA$ . Fortunately, an analytical solution by (Mueller, 2007, § 3.2.3.e) solves these scattered orders, resulting in a single expression that is reasonably inexpensive to compute.

$$F(\lambda) = \frac{\epsilon}{\pi\Delta^2} \int_A \left[ m_O(\vec{r}) + \frac{\mu_O(1-\epsilon)\sin^2(\gamma/4)\cos^2(\gamma/4)}{1-(1-\epsilon)\sin^2(\gamma/4)} \right] B(\lambda, T(\vec{r})) dA \quad (\text{Mueller, 3.46})$$

This expression includes the emissivity,  $\epsilon$ ; distance to the observer,  $\Delta$ ; the cosine,  $m_O$ , of the angle between the observer and the normal,  $\vec{r}$ , to the facet; and the cosine,  $\mu_O$ , of the zenith angle to the observer from the facet; as well as a number of trigonometric operations involving the crater opening angle,  $\gamma$ . Fundamentally, these act as a scaling factor on the Planck function, which determines the flux density,  $B_\lambda(T)$  emitted at some wavelength  $\lambda$  by a blackbody of some temperature  $T$ :

$$B_\lambda(T) = \frac{2hc^2}{\lambda^5(e^{hc/k_B\lambda T} - 1)} \quad (4.6)$$

where  $h$  is Planck's constant,  $c$  is the speed of light, and  $k_B$  is the Boltzmann constant (Petty, 2006).

Equation Mueller, 3.46 returns the observed flux from all subfacets within one facet. This process is repeated for all facets within the observation footprint, and the observed flux from each facet is summed to produce the total observed flux for some wavelength. The whole process is then repeated, from the point after the facets' temperatures were determined, for each wavelength in question. These fluxes are then recorded for analysis.

### 4.1.6 Model Output

Once the model has determined the temperature for each facet, it calculates and outputs the observed flux. Specifically, it finds the flux density at each wavelength of interest that arrives at the observer from each facet, then sums together these contributions to find the total. Thus, for a given observation and wavelength, this gives a total flux density in Janskys ( $10^{-26} \text{ W m}^{-2} \text{ Hz}^{-1}$ ). The choice of Janskys as an output unit is a result of the model's original development for unresolved observations of asteroids.

The Jansky is a measure of radiance per unit wavelength, whereas TES uses radiance per unit wavenumber—i.e.,  $\text{W cm}^{-2} \text{ sr}^{-1} \text{ cm}^{-1}$ . Rather than convert between the two, once the model outputs a simulated flux measurement at some wavelength, we then convert this into a brightness temperature for comparison with the corresponding TES observation. This is found by the following relation:

$$T_b = \frac{hc}{k\lambda} \left( \ln \left( 1 + \frac{2hc^2}{I_\lambda \lambda^5} \right) \right)^{-1} \quad (4.7)$$

where  $T_b$  is brightness temperature in Kelvin,  $h$  is the Planck constant,  $c$  is the speed of light,  $k$  is the Boltzmann constant,  $\lambda$  is the wavelength of the observation, and  $I_\lambda$  is the radiance per unit wavelength (Petty, 2006).

This allows for direct comparison to TES observations, which have also been reported in brightness temperature (Christensen et al., 2001). As TES brightness temperatures are derived from radiance per unit wavenumber, the relationship is slightly different:

$$T_b = \frac{hc\nu}{k} \left( \ln \left( 1 + \frac{2hc^2\nu^3}{I_\nu} \right) \right)^{-1} \quad (4.8)$$

where  $\nu$  is the wavenumber of the observation,  $I_\nu$  is the radiance per unit wavenumber, and all other terms are defined as above (Petty, 2006).

## 4.2 Modifications to the Model

As Convex was developed for unresolved observations of asteroids (Mueller, 2007), several important considerations needed to be accounted for when modifying it for use with Phobos. Foremost was the presence of Mars, which, as viewed from Phobos, presents a disk over  $40^\circ$  across, occupying  $\sim 0.4$  steradians of Phobos' sky ( $\sim 6.3\%$ ).

Mars contributes to the thermal environment of Phobos in three key ways:

1. During some seasons, Phobos passes into the shadow of Mars on each orbit. These eclipses block Sun light from reaching Phobos for a portion of its orbit, creating distinct temperature dips.
2. Mars reflects sunlight, some of which is radiated onto the surface of Phobos.
3. Mars emits thermal energy as infrared radiation which is radiated onto the surface of Phobos.

Each of these effects was taken into account in PhobosTPM.

### 4.2.1 Eclipsing

The intersection of Phobos' orbit with the ecliptic forms a line that points in some fixed direction. As Mars circles the Sun, whenever the angle between this direction and the Sun is less than the apparent angular radius of Mars, the Sun, as viewed by Phobos, is blocked by Mars. In other words, Phobos passes through Mars' shadow. The timing of these eclipses is organized in two seasons, each centered around Mars' equinoxes. The northern spring eclipse season lasts from  $L_s = 300.4 - 56.8$ , and the northern autumn eclipse season lasts from  $L_s = 120.9 - 244.1$  (Pratt & Hopkins, 2011). Combined, these eclipse seasons represent a majority of the year ( $\sim 66\%$ ). The duration of these eclipses varies, but can last up to 54 minutes, or  $\sim 12\%$  of every orbit (Kuzmin & Zabalueva, 2003). The observations used in

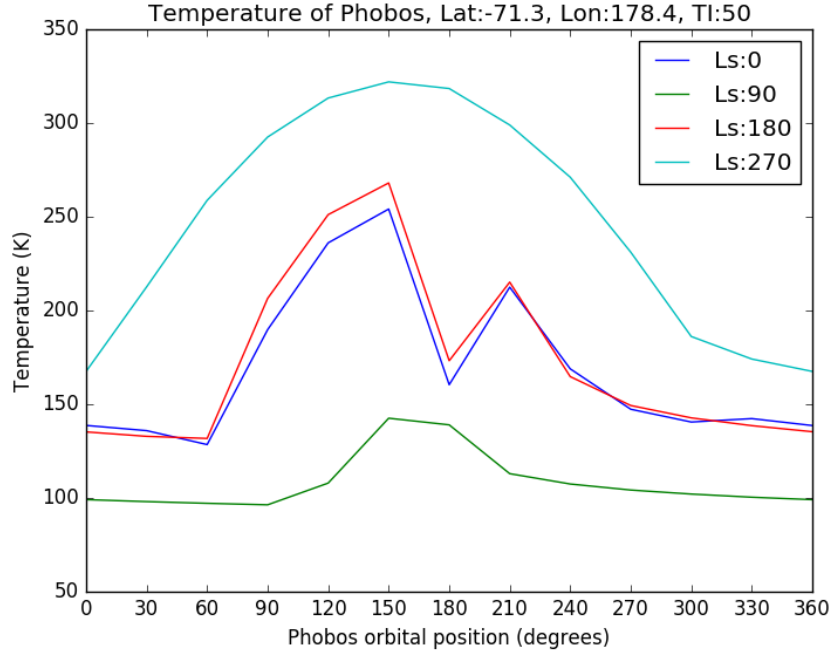


Figure 4.1 Temperature over the course of one orbit for a facet near Phobos’ southern pole, assuming a thermal inertia of  $50 \text{ J m}^{-2} \text{ K}^{-1} \text{ s}^{-1/2}$ . The four curves each represent one season, at  $L_s = 0, 90, 180,$  and  $270$ . Note that near the Martian equinoxes at  $L_s = 0$  and  $180$ , a large bite is taken out of the afternoon high temperatures, as Phobos enters, and subsequently exits, the shadow of Mars.

this work, described in Chapter 3 and summarized in Table 3.1, all fell within the northern spring eclipse season. Though our observations were not collected during eclipse itself, we felt it important to include this effect for completeness.

Eclipsing was incorporated into the PhobosTPM model by turning off incident solar radiation for any time step in which the Sun-Phobos-Mars angle was smaller than the angular radius of Mars from Phobos. The apparent disk of Mars from Phobos grows and shrinks slightly due to Phobos’ orbital eccentricity. As illustrated in Figure 4.2, the true angular radius,  $\theta$ , can be calculated from Mars’ radius,  $r_m$ , and Phobos’ orbital distance,  $d$ , using

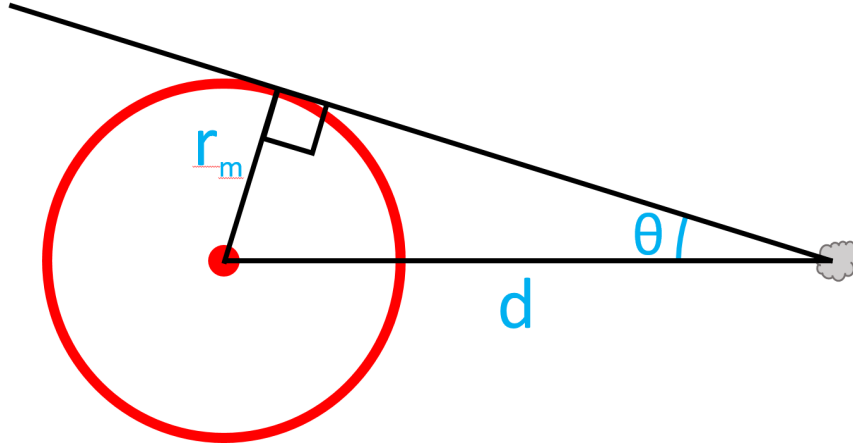


Figure 4.2 Definition of angles and distances used to calculate the angular size of Mars, viewed from Phobos. When the Sun-Phobos-Mars angle is smaller than the angular radius of Mars, our model turns off solar illumination, simulating an eclipse of the Sun by Mars, as viewed from Phobos. Mars' angular radius,  $\theta$ , can be found using equation 4.9.

the following trigonometric relationship:

$$\theta = \arcsin \frac{r_m}{d} \quad (4.9)$$

Based on Mars' equatorial radius of 3396.3 km, and Phobos' periapsis of 9234.4 km, and apoapsis of 9517.6 km,  $\theta$  varies by 3.2%, between 20.9° and 21.6°. Mars was assumed to have a circular apparent disk with constant angular radius of 22°, essentially assuming Phobos to have a circular orbit.

This implementation also ignores the apparent disk of the Sun, assuming it to be a point source of illumination (as is assumed throughout the model). However, at the orbit of Mars, the sun's angular radius is a mere 0.175°, so periods of partial eclipse are sufficiently small as to be ignored in the interest of computational efficiency.

## 4.2.2 Mars-Shine

To include the effects of scattered and emitted radiation from Mars (collectively, “Mars-shine”), we used a Mars global climate model to determine the solar flux scattered back to space and the thermal infrared flux emitted back to space from selected points on Mars’ surface. Using the geometry of the Mars-Phobos system, a diurnal curve was computed describing the average total Mars-shine flux over the course of one orbit (Figure 4.3). Mars-shine varies somewhat with Mars’ solar longitude,  $L_s$ , which was also taken into account in our model.

### The Mars Climate Database (MCD)

We made use of the Laboratoire de Météorologie Dynamique (LMD) Mars Climate Database (MCD) (Lewis et al., 1999; Millour et al., 2015) for this work. The MCD is a database of Mars atmosphere statistics, which is queryable for any position on Mars’ surface, and upwards through the atmosphere to an altitude of  $\sim 300$  km. The statistics comprising this database were generated by the LMD Global Climate Model (GCM), which simulates physical and chemical processes throughout the Martian atmosphere. Mars’ water cycle,  $\text{CO}_2$  cycle, dust transport mechanisms, high-altitude photochemical processes, and more are modeled in high resolution by the GCM, in order to accurately simulate the forces governing Mars’ climate. It has been robustly vetted against the available record of atmospheric observations.

In addition to the familiar weather-related outputs such as temperature, pressure, wind speed, and atmospheric composition, the LMD also reports how much solar energy per square meter is scattered back to space by Mars at a given time and location at the top of the atmosphere, and how much energy per square meter is thermally radiated away to space. It is these two variables that we sought to determine in order to accurately model the influence of Mars on the thermal environment of Phobos.

## Mars-Shine Calculation

When calculating Mars-shine, for simplicity, Phobos' orbit was idealized as perfectly circular and equatorial, with a radius equal to its true semimajor axis, 9378 km. Mars was idealized as a sphere using Mars' equatorial radius, 3396.2 km. For 12 time steps along Phobos' orbit, 3000 points were selected within the portion of Mars visible from Phobos. These points were randomly selected uniformly in angular space as viewed from Phobos.

Each point was passed to the MCD, and 24 time steps were queried to construct a diurnal curve representing the thermal and reflected flux from that point to space. Each diurnal curve was shifted in time to represent the difference in local solar time between points at different longitudes. Once all diurnal curves were aligned to the local time at the center of the observed region, the diurnal curve of total flux at the position of Phobos was calculated, assigning each point a solid angle of 1/3000th of the total solid angle subtended by the visible region of Mars. In essence, rather than analytically integrate the contributions of each observed portion of Mars, the integration was performed statistically. The thermal and reflected solar components were summed to a single flux value, representing the total flux from Mars arriving at Phobos.

This resulted in a diurnal curve for each position along Phobos orbit, each with small variations based on the albedo and thermal inertia of the Martian surface visible below that orbital position. These 12 diurnal curves, each comprised of 24 time steps, were then averaged into a single diurnal curve, and interpolated using a cubic spline fit to produce a function. This function represented the average flux received by Phobos from Mars at every point along its orbit (i.e., at every time throughout Phobos' "day"). As Mars-shine is dependant on season, this process was repeated to produce a Mars-shine function for each Mars solar longitude for which thermophysical modeling of Phobos was performed, including the  $L_s$  of each set of TES observations, summarized in Table 3.1.

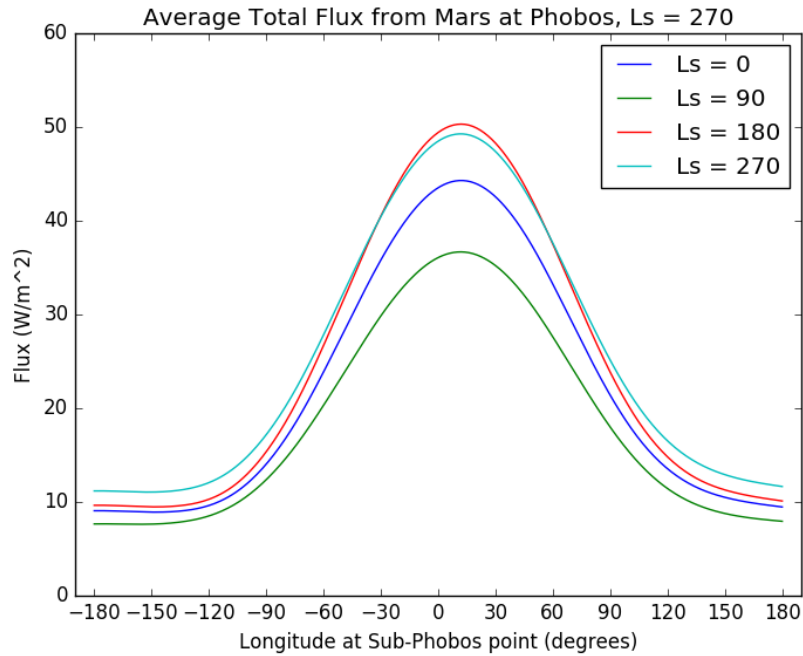


Figure 4.3 Total flux originating at Mars at the orbit of Phobos. The horizontal axis marks the position of Phobos along its orbit, with respect to Mars, with 0 Longitude marking Mars' sub-solar point. As there is some variation in this curve depending on Mars surface albedo and thermal inertia features, each curve shown above is an average of 12 diurnal curves centered over Mars regions at 30 degree longitude intervals. The curves shown are cubic spline fits to the computed averages representing the average Mars-shine over the course of one Phobos orbit at four selected Mars  $L_s$ . Note that the peak flux is experienced slightly past the subsolar point, a result of higher afternoon temperatures due to the effect of the thermal inertia of the Martian surface. For comparison, the flux arriving from the Sun at Phobos varies throughout the year, between a maximum of  $713 \text{ W/m}^2$ , at  $L_s = 251$ , and minimum of  $490 \text{ W/m}^2$ , at  $L_s = 71$ .

## Integration with PhobosTPM

Each function was added to PhobosTPM to be called upon based on the Mars solar longitude being modeled. PhobosTPM accounts for Mars-shine as an additional point illumination source centered at the center of Mars. This position is held constant relative to Phobos, as Phobos is tidally locked, and the flux is varied according to the Mars-shine function. The position of the “Sun” illumination source revolves around the whole configuration, with the Sun’s position determining where in the Mars-shine function to set the Mars-shine flux.

This method does have the limitation of not taking into account the spatial extent of Mars. Inside PhobosTPM, the energy transmitted by Mars-shine is cut off once the point illumination source drops below the horizon. In reality, the  $\sim 40$  degree disk of Mars would sink below the horizon, slowly reducing the transmitted energy with increased latitude away from Phobos equator. The small scale of Mars-shine compared to the influence of solar radiation is at its greatest near the poles, but this is also where we expect this point-source illumination effect to have its greatest difficulty representing the real Mars-shine. A more accurate representation was found to be too computationally expensive to implement. The regions observed by TES were not near enough to the poles for this effect to significantly influence our result.

### 4.2.3 Phobos Shape Model

Functionality was added to read in a Phobos shape model comprised of 49,152 triangular facets (Gaskell, 2011). Each facet was approximately  $\sim 200$  m in extent. Higher-resolution models were available in the same dataset, but we employed the 49,152-facet model<sup>3</sup>, which was able to achieve resolution exceeding our highest-resolution TES observations by a factor of  $\sim 10$ . In addition, this model’s triangular facets interfaced natively with our thermal

---

<sup>3</sup>PDS Data Set ID: V01-SA-VISA/VISB-5-PHOBOSHAPE-V1.0, Product ID: PHOBOS\_VERTEX\_VER64Q-TAB.

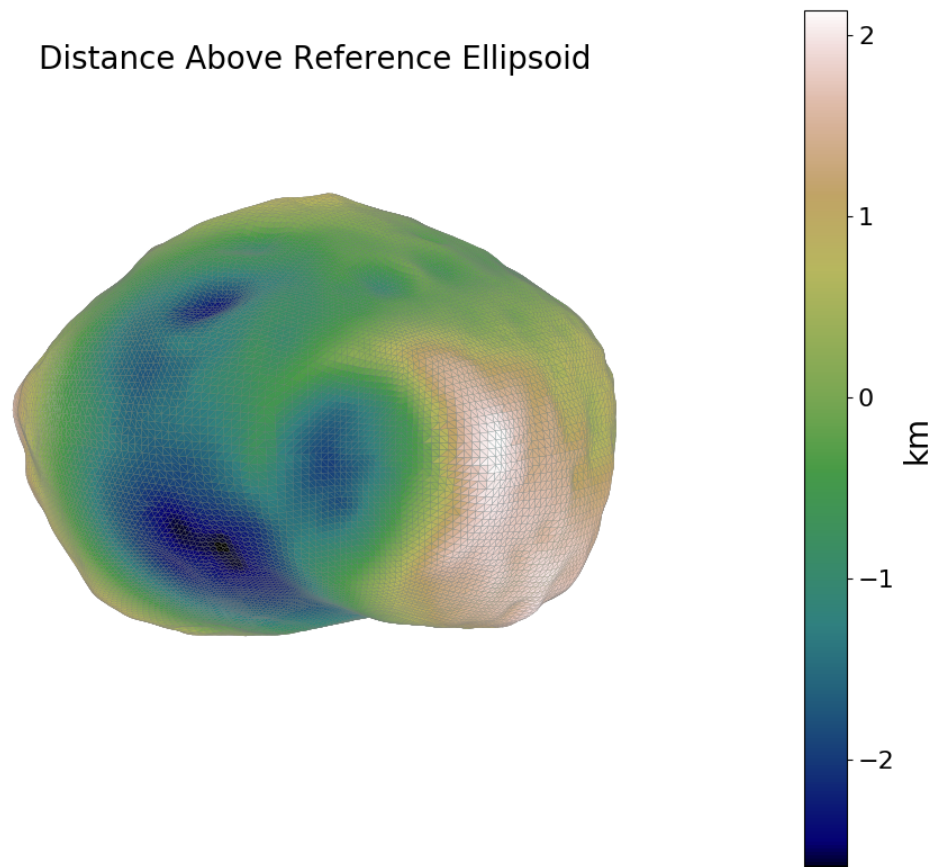


Figure 4.4 Elevation difference between Gaskell (2011) Phobos shape model and predicted distance from center according to tri-axial ellipsoid. Ellipsoid radii are  $13.03 \times 11.40 \times 9.14$  km, from Willner et al. (2014). Notice the maximum distance above reference ellipsoid, in white, just east of Stickney crater (lower right), and the maximum distance below reference ellipsoid, in dark blue, across the southern polar region.

model, unlike other options which use implicitly connected quadrilateral facets.

Previous modelers (e.g., Kührt & Giese (1989), Kuzmin & Zabalueva (2003)) have used the tri-axial ellipsoid approximation as a simplification for computation and due to the unavailability of high-resolution shape modeling at the time. Not only does the use of the shape model improve our ability to model temperatures within the regions observed by TES, but it allows us to prepare global temperature maps with distinguishable surface features.

Figure 4.4 demonstrates the the Gaskell (2011) shape model’s improvement over a tri-

axial ellipsoid approximation based on recent measurements of Phobos' principle axes (Willner et al., 2014).

#### **4.2.4 Integration of Flux within FOV**

Convex was developed for unresolved asteroid observations. This means flux from the entire visible portion of the asteroid must be integrated into a single point source. As described in Section 4.1.5, the integration is performed natively by the model, as flux from each facet of the modeled object is summed up when each wavelength's flux density is reported.

Because we compare the results of our model with resolved observations of Phobos by TES, the detector's field of view only collects flux from a portion of Phobos' surface. To restrict the model to only integrate flux from facets within the field of view, we simply restrict the shape model input to PhobosTPM to the set of facets within that observation footprint. As our model already ignores radiation of heat between facets, we lose no fidelity by excluding facets beyond the field of view. As a side benefit, we also significantly improve computation time, as we do not need to compute the temperatures of and emissions from the vast majority of facets making up the object.

#### **4.2.5 Geometry of Illumination Sources and Observer**

An additional change was made in the way the model handles the geometry of each object being modeled. This came about due to the unique circumstance of Phobos experiencing Mars-shine compared to free-floating asteroids, as well as the unique observations being modeled, which were from close proximity to the target, compared with observations of asteroids made from distances of tens or hundreds of millions of kilometers.

In the original Convex model, the placement of both the target asteroid and the observer were specified using heliocentric coordinates, i.e., heliocentric distance, ecliptic longitude,

and ecliptic latitude. Once the target asteroid was constructed and the Sun and observer were placed, the Sun and observer would revolve around the center of the asteroid to simulate the rotation of the asteroid.

In PhobosTPM, the placement of the Sun, Mars, and TES instrument with respect to Phobos were specified as 3 dimensional vectors in the Phobos-centered Cartesian coordinate system. Phobos' rotation with respect to the Sun is then simulated by revolving the Sun around the center of Phobos. However, in this case, the positions of Mars and TES remain fixed, as Phobos is tidally locked to Mars.

### 4.3 Model Iterations

We selected 9 wavelengths to query across each model instance. These were chosen to be roughly logarithmically spaced over the wavelength range of the TES instrument's sensitivity. This was done to correspond to the spacing of TES's spectral channels, which were distributed evenly in wavenumber space. The wavelengths we selected were 8, 10, 12, 14, 17, 20, 25, 30, and 45 microns. In wavenumber, this translates to 222, 333, 400, 500, 588, 714, 833, 1000, and 1250  $\text{cm}^{-1}$ .

Our primary variable of interest to this investigation was thermal inertia. We aimed to map the spatial variation of thermal inertia across Phobos' surface. As such, we tested many different values to initially refine a range that was most likely to represent the true physical characteristics of the surface of Phobos. Previous authors have estimated Phobos' thermal inertia to be anywhere from 15  $\text{J m}^{-2} \text{K}^{-1} \text{s}^{-1/2}$  (Gatley et al., 1974) up to 150  $\text{J m}^{-2} \text{K}^{-1} \text{s}^{-1/2}$  (Bandfield et al., 2018) (see Table 2.1).

Ultimately, we modeled our observations using six different thermal inertias, spaced roughly logarithmically due to the decreasing sensitivity of temperature to thermal inertia at increasing thermal inertias. The values we used were 10, 25, 50, 85, 130, and 250  $\text{J m}^{-2}$

$\text{K}^{-1} \text{s}^{-1/2}$ . At the spatial scales we are investigating, we do not expect our results to diverge greatly from prior estimates of Phobos' global average thermal inertia. We have therefore modeled only thermal inertias between 10 and  $250 \text{ J m}^{-2} \text{ K}^{-1} \text{ s}^{-1/2}$ , and assume results beyond this range to be inconsistent with Phobos' true thermophysical properties. However, we do not rule out smaller-scale features, below the spatial resolution of our observations, with higher thermal inertia.

Each of the six thermal inertia conditions was also paired with one of four surface roughness conditions (zero, low, medium, and high), as described in Section 4.1.3 and Table 4.1. This gave a total of 24 possible surface conditions. These 24 surface conditions were applied to each of 356 observation regions, resulting in a total of 8544 model instances. Reporting the flux density for each of the 9 selected wavelengths, across these 8544 instances, the model ultimately evaluated 76,896 individual fluxes. Processing these instances took 2711 CPU hours of computation time, or just over 16 CPU weeks.

Computation for this project was carried out on Northern Arizona University's High Performance Computing cluster, Monsoon, which afforded the ability to run many model instances in parallel. Thanks to that resource, the calendar time required to complete our modeling runs was only a few days.

## 4.4 Derivation of Observed Thermal Inertia

We wish to apply our modeling to derive the thermal inertia that best reproduces the observed brightness temperature spectrum. To accomplish this, we interpolate the six brightness temperatures determined by our model instances with six different thermal inertias to functionally express the expected brightness temperature given any thermal inertia. Then we simply solve this function for the observed brightness temperature, giving us the thermal inertia corresponding to our measurement.

Comparison of Modeled and Observed Brightness Temperature

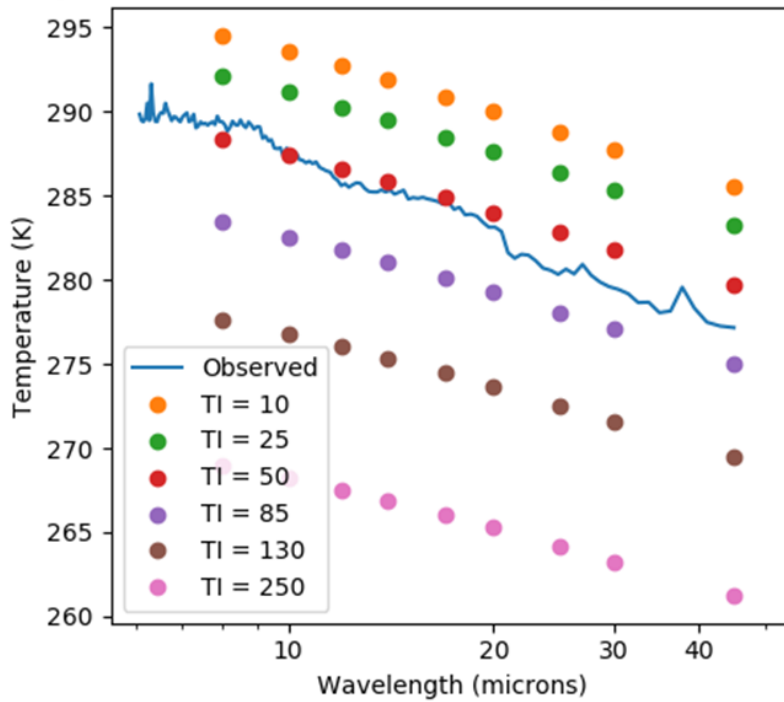


Figure 4.5 Comparison of Modeled and Observed Brightness Temperature. Each instance of the model (points) assumed a different thermal inertia (TI), producing a different curve for simulated brightness temperature over wavelength. Comparing these model results with the observed TES brightness temperature spectrum (line), we can find the thermal inertia that best reproduces each observation. This determination of thermal inertia is dependent on wavelength, as discussed in Section 6.1.2.

As both the observed and modeled brightness temperature vary with wavelength, the thermal inertia determined using this method will be wavelength dependent as well, as discussed in Section 6.1.2. We found the best thermal inertia for nine wavelengths within the observed spectrum (8, 10, 12, 14, 17, 20, 25, 30 and 45  $\mu\text{m}$ ), yielding an independently determined thermal inertia at each wavelength.

# Chapter 5

## Results

Out of our 356 observations (see Section 3.5), a total of 181 produced a valid thermal inertia by the method described in Section 4.4. This means our modeling was unable to reproduce 175 observations using any TI within the modeled range. A quality selection cut was made to select observations between LST = 1900 – 0600, as detailed in Section 6.1.1. This further reduced the number of observations included in our analysis to 103. Based on 94 of these observations made at 10  $\mu\text{m}$ , we derive an average thermal inertia of  $42 \pm 13 \text{ J m}^{-2} \text{ K}^{-1} \text{ s}^{-1/2}$  (Section 5.1) and map how this thermal inertia varies over the observed region (Section 5.2).

### 5.1 Average Thermal Inertia of Phobos

Table 5.1 summarizes the reduced results of our modeling. Between 8 – 20  $\mu\text{m}$ , over 90 observations at LST 1900 – 0600 produced valid thermal inertias at each wavelength.

If we treat the two highest points in the distribution as outliers (as they appear to be as seen in Figure 6.4), then the 10  $\mu\text{m}$  thermal inertia takes on a mean of  $42.0 \text{ J m}^{-2} \text{ K}^{-1} \text{ s}^{-1/2}$ , with a standard deviation of 13.6 ( $N = 94$ ). 90% of these observations fall between 20

Table 5.1 Statistics of Thermal Inertia Distributions at Nine Wavelengths

Wavelength	N	Mean	St. Dev.	5 %ile	95 %ile	Min	Max
8 $\mu\text{m}$	94	92.3	39.1	41.0	160.7	30.9	223.4
10 $\mu\text{m}$	96	45.8	29.5	21.7	62.7	16.3	246.7
12 $\mu\text{m}$	95	30.8	10.6	14.9	41.8	11.3	82.1
14 $\mu\text{m}$	96	24.4	6.6	14.5	32.8	10.4	42.5
17 $\mu\text{m}$	95	19.9	5.4	11.6	26.8	10.4	41.4
20 $\mu\text{m}$	92	18.4	5.4	11.7	23.8	10.1	42.9
25 $\mu\text{m}$	82	17.7	6.4	10.8	22.0	10.0	52.8
30 $\mu\text{m}$	71	17.3	7.1	11.3	22.0	10.6	58.3
45 $\mu\text{m}$	63	16.3	11.5	10.6	28.0	10.0	82.7

Note. — N is the number of observations which produced a valid thermal inertia at that wavelength. Mean, standard deviation, percentiles, minimum, and maximum are given in thermal inertia’s units of  $\text{J m}^{-2} \text{K}^{-1} \text{s}^{-1/2}$ .

– 60  $\text{J m}^{-2} \text{K}^{-1} \text{s}^{-1/2}$ . A histogram of the distribution of these 94 thermal inertias is shown in Figure 5.1.

## 5.2 Mapping the Thermal Inertia of Phobos

Each of the 94 observations used generated an independently determined thermal inertia. Any given location within the observed region may have been observed multiple times. To map out any spatial variations in thermal inertia across the surface of Phobos, we ask, for each facet, what observations that facet fell in, then find the median thermal inertia of all of those observations.<sup>1</sup> This gives us, for each facet, the average thermal inertia across all observations. We then can create a map showing how thermal inertia varies across Phobos, shown in 3-dimensions in Figure 5.2, and as a 2-dimensional map in Figure 5.3.

The observations with the lowest TIs were found generally in the western mid-latitudes of Phobos’ trailing hemisphere, and higher TIs were found almost exclusively in the south-

<sup>1</sup>We use the median to help suppress the effects of outliers in our data.

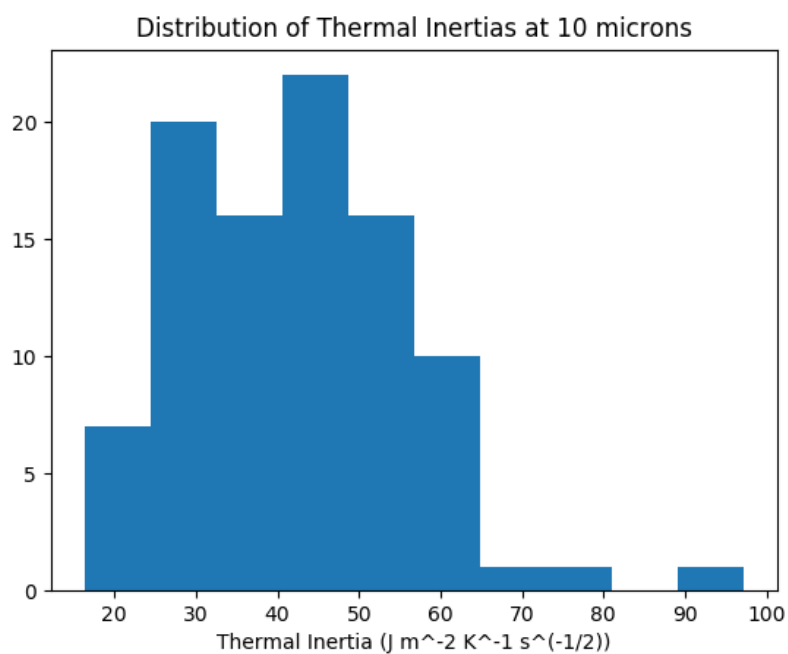


Figure 5.1 Thermal inertia (TI) determined at 10  $\mu\text{m}$  for 94 observations between 1900 – 0600 LST at the observation center. Note the fairly normal distribution around the mean of  $\sim 42 \text{ J m}^{-2} \text{ K}^{-1} \text{ s}^{-1/2}$ .

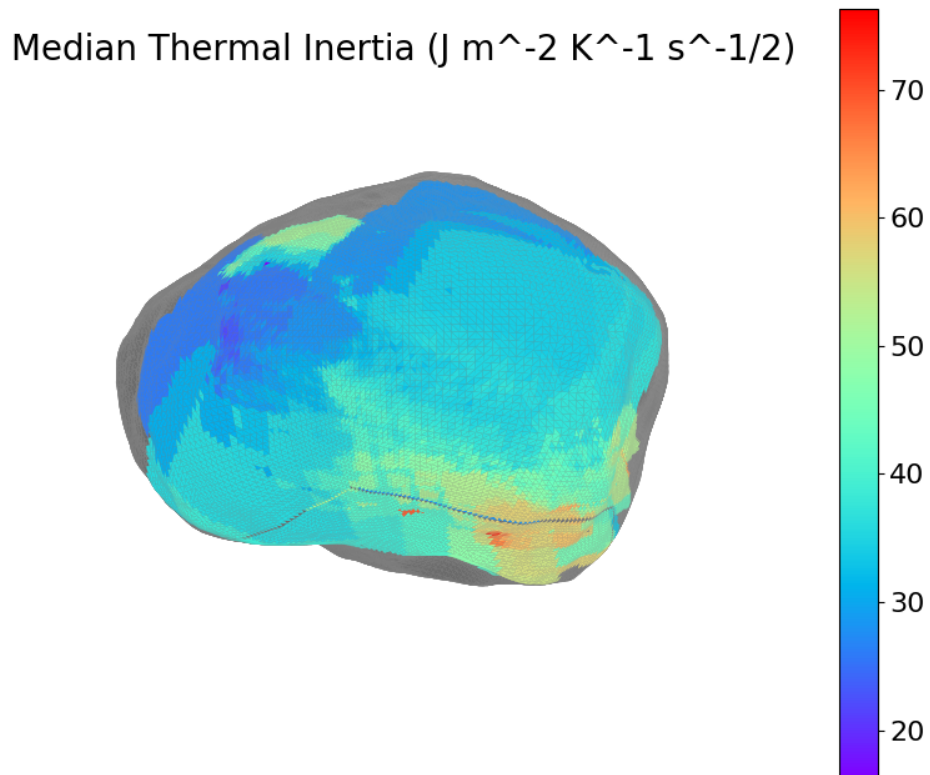


Figure 5.2 Thermal inertia for each observed facet, averaged over all observations of that facet, as determined at 10 microns, with medium surface roughness. This is the trailing hemisphere, as Phobos orbits, with the sub-Mars point being on the left in this figure.

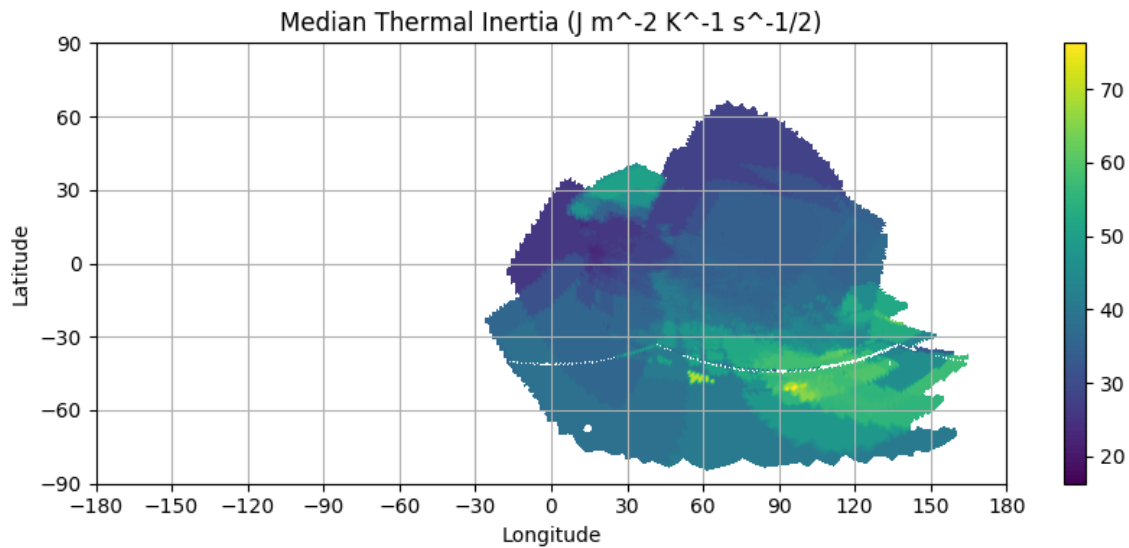


Figure 5.3 Thermal inertia for each observed facet, averaged over all observations of that facet, as determined at 10 microns, with medium surface roughness. This map shows the same information as Figure 5.2, in a format that corresponds to previous maps shown in this work, such as Figure 1.2.

ern polar region. We believe this results from some surfaces remaining illuminated in the southern polar region throughout our observations, despite filtering our data by local solar time to eliminate daytime observations.

By averaging together all observations of a given facet, we have a better sense of how TI varies across the surface of the observed region. This tells us that the thermal inertia is largely uniform, at least to our ability to measure.

# Chapter 6

## Analysis and Discussion

Each TES observation was found to produce a trend in brightness temperature over wavelength, as seen, for example, in the blue spectrum in Figure 4.5. This can be interpreted as each observation having a mixture of temperatures within each footprint, as a result of topography, illumination geometry, and surface roughness creating small shadows and hotspots. Our model produces a single surface temperature for each facet, but as each observation is composed of hundreds or even thousands of facets, it can begin to capture this effect, as seen in the colored points in Figure 4.5. Longer wavelengths probe slightly deeper into the subsurface, which will also have different temperatures.

### 6.1 Analysis

Our model was able to reproduce some observations quite well, with all wavelengths being well fit with a single thermal inertia. Others showed a steep trend in thermal inertia, with short and long wavelengths being fit with widely different TIs. Still other observations were so unruly that the observed brightness temperature could not be reproduced by the model, with the model either producing temperatures much higher or much lower than the

observation.

In light of the fact that so many of our observations failed to be fit by any combination of model parameters, we sought to determine what might explain this troublesome result.

### 6.1.1 Local Solar Time Dependence of Thermal Inertia

We began by plotting the dependence of thermal inertia on Local Solar Time (LST). In principle, thermal inertia has no reason to vary with LST, though, given our set of observations, it is possible that a correlation between the two might result from a true spatial variation in TI across the surface of Phobos as a result of observational biases. However, our null hypothesis remained that thermal inertia was, to first order, constant across Phobos.

A systematic error in thermal inertia could arise with a local time dependence due to the way temperature varies with time on airless bodies. As shown in Figure 6.1, thermal inertia is best distinguished by temperature during the over-night hours, when temperature slowly decreases after sunset and throughout the night. This means that the most accurate determinations of TI will be between  $LST = 1800 - 0600$ . During the day, temperature changes quickly, and at early morning and mid-afternoon there is a period during which many different thermal inertias will produce the same temperature.

To investigate the possibility of such a systematic error, we determined the median solar time of each observation, using the LST of each facet within that observation footprint. Figure 6.2 shows the relationship between thermal inertia and LST, using the TI determined at  $10 \mu\text{m}$ . At this wavelength, there were many observations for which no thermal inertia was found that reproduced the observed brightness temperature. These un-matched observations were assigned a TI of -1 to distinguish them in this figure, and they can be seen in a horizontal line across the lower portion of the plot. The horizontal axis spans the range of local times from 0000 LST (local midnight) through the daylight hours and back to 2400 LST (midnight

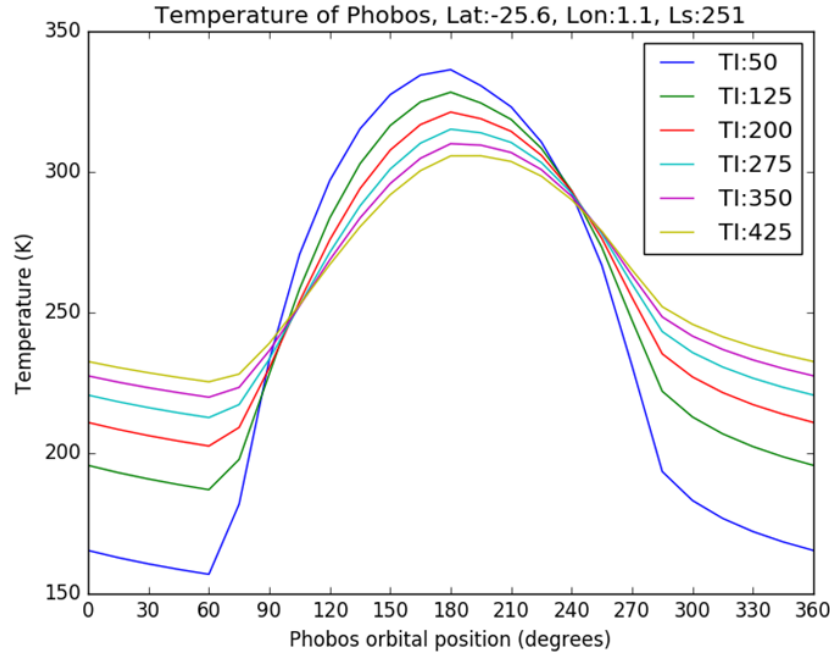


Figure 6.1 Modeled temperature of a representative location near Phobos' equator, at perihelion.

again). Our observations range from  $\sim 0900$  LST, through midnight, to  $\sim 0300$  LST.

As demonstrated by the density of points along the  $TI = -1$  line, the majority of modeling failures occurred during the daylight hours and into the early evening. Beyond about 1900 LST or so, the model successfully determines a TI match to observations throughout the overnight hours. This matches our expectations, given the above discussion of the expected dependence on TI of the diurnal temperature curve. In fact, the vertical grouping of points near 1400 LST is a consequence of many TIs producing the same temperature in the mid-afternoon portion of the diurnal temperature curve. The remaining outliers in the overnight portion of the data may be the result of observations near the south pole, where several regions remained illuminated throughout the night.

Figure 6.3 confirms that the identified dependence of TI on LST holds true for all wavelengths. In this figure, we show LST centered at 1800 hr, rather than noon, to keep our data

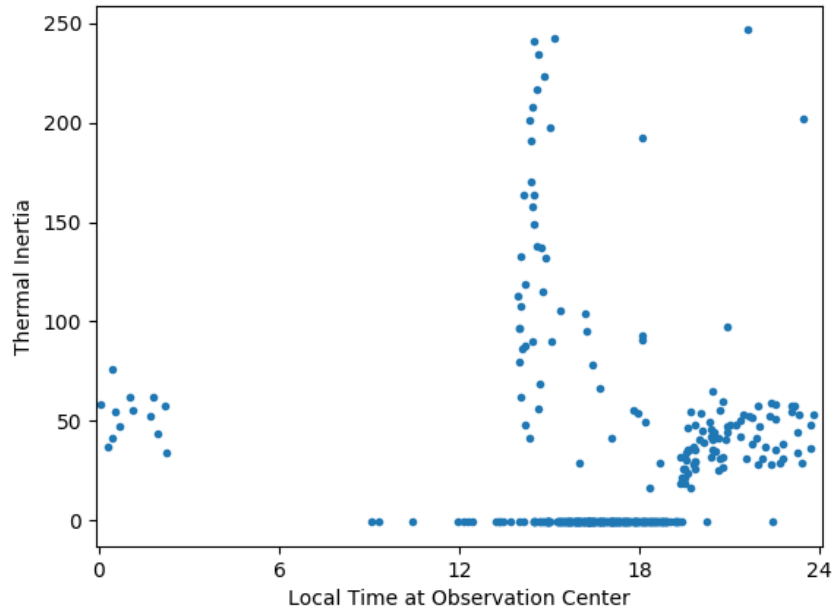


Figure 6.2 Thermal inertia (TI) as determined from  $10\ \mu\text{m}$  observations plotted against local solar time (LST) at the center of that observation. Observations for which no thermal inertia could be determined were assigned a value of -1, and are seen along the bottom of the figure. No trend between TI and LST is expected, though one could imagine a true spatial variation in thermal inertia across the observed region. We interpret the observed clustering to be the result of systematic errors affecting our TI determination for observations of sunlit regions. Observations between 1900 – 0500 LST demonstrate a clear agreement in TI between  $30 - 70\ \text{J m}^{-2}\ \text{K}^{-1}\ \text{s}^{-1/2}$ .

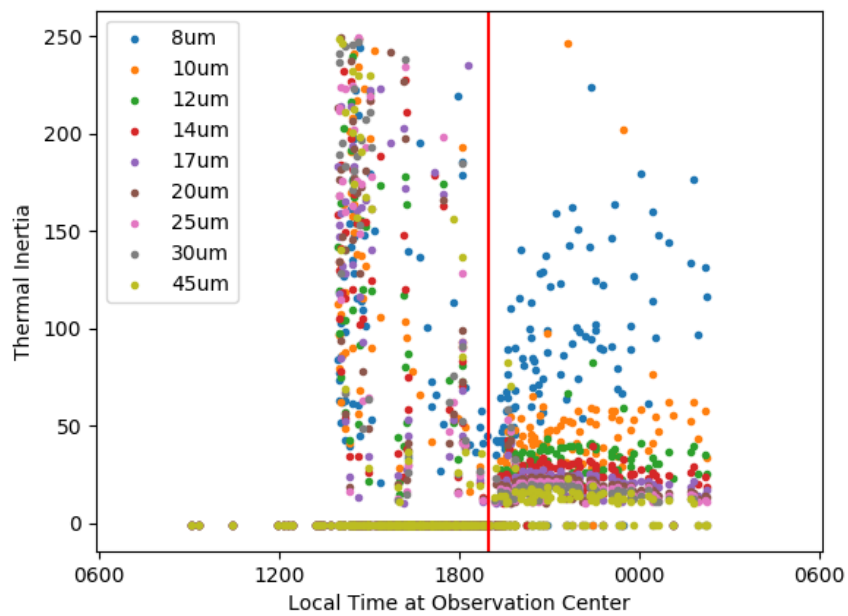


Figure 6.3 Thermal inertia (TI) as determined from observations at all 9 modeled wavelengths plotted against local solar time (LST) at the center of that observation. The systematic errors found in the 10  $\mu\text{m}$  modeling, in Figure 6.2, above, hold true across all wavelengths. We now make a cut across LST in order to examine trends in TI with wavelength in more detail.

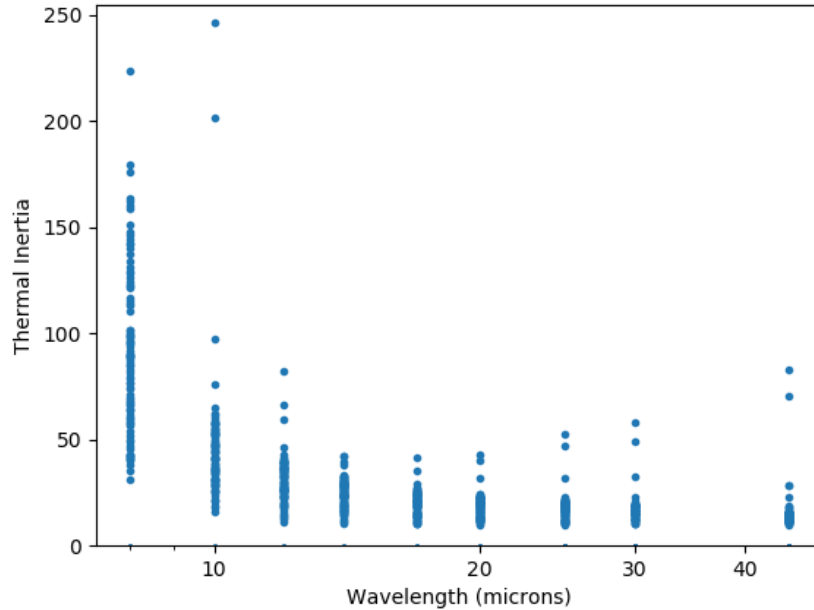


Figure 6.4 Thermal inertia (TI) vs wavelength, data clipped using local solar time (LST) = 1900 – 0600 at the observation center.

together. The red vertical line at 1900 hr demarcates the selected cut we used to reject TIs that fall prey to the systematic error identified above. At local times earlier than 1900 hr, the determined TIs appear to have no correlation with wavelength, and a great number of observations produced no TI determinations whatsoever. After 1900 hr, nearly all observations were fit with valid thermal inertias at many or all wavelengths. These TIs remain do not trend up or down with local time after 1900 hr, though they can be seen to trend with wavelength, as discussed in Section 6.1.2, below.

### 6.1.2 Wavelength Dependence of Thermal Inertia

A consistent trend was found resulting generally in a higher TI at shorter wavelengths for each observation, as seen in Figure 6.4. This trend was somewhat puzzling, and we considered several possible explanations.

Does the observed trend imply that TI changes with depth? One would assume that longer wavelengths probe deeper into the subsurface, and that TI might well increase with depth as the material becomes more compacted. However, this would produce the opposite trend than we observe, with TI increasing at longer wavelengths.

Might these results be influenced by the inability of smaller particles to emit at longer wavelengths than their own size? If this were the case, then if the surface were mostly small particles, emission at longer wavelengths would be suppressed. This would create an additional dampening on the determined thermal inertia during night-time observations at long wavelengths, as low emission is interpreted as low temperature, which, at night, would be consistent with low thermal inertia. Conversely, one might argue that looking at longer wavelengths, one will only see the effects of larger particles. Therefore, one might expect that these larger particles ought to create an increase in determined thermal inertia by nature of their size, regardless of their abundance in the observed region.

So far, the interpretation of the decrease of TI with wavelength is inconclusive. In the following sections, we apply the TI determined at  $10\ \mu\text{m}$  for our remaining analysis.

## 6.2 Limitations

It is important to note the limitations of our model when interpreting our results. Being a 1-dimensional thermal model, it does not take into account shadowing of facets by other facets, nor absorption of radiation from one facet by another. It also produces only a single surface temperature for each facet. Any conditions that would produce a mixture of temperatures at the scale of a single facet or smaller (i.e., less than  $\sim 100\ \text{m}$ ) are not accounted for by our model. For instance, Phobos is known to have large rocks and boulders across its surface, which are not explicitly taken into account (Thomas et al., 2000). Large rocks, having a higher thermal inertia than their surroundings, would release their stored heat

slowly throughout the night, increasing the effective thermal inertia of the surrounding area.

During the day, temperature at the surface changes quickly, often fast enough that there is a significant difference in temperature between two neighboring facets. This would imply a gradient in temperature across each facet that is not captured by the single temperature derived by our model.

In addition, near the terminator, surface roughness and rock abundance create long shadows across the surface that lower the temperature at sub-facet scales. While our model uses hemispherical cratering to account for surface roughness when calculating emission, it does not produce sub-facet variations in temperature that would result from this effect.

Furthermore, small uncertainties in the position of a TES observation footprint produce some uncertainty in local solar time. When temperature changes quickly (that is, during the day), this can result in a poor match between model and observation.

Luckily, we can work around these weaknesses by concentrating on observations of the night side of Phobos, where temperature changes slowly, and thermal inertia is the greatest influence on temperature, as seen in Figure 6.1. Those observations that our model was unable to reproduce (those seen in the horizontal stripe across the bottom of Figure 6.3) are nearly all found on the sunlit side of the body.

Each of our three sets of observations was made at nearly the same location in Phobos' orbit, as seen in Figure 3.1. This means that regions that were sunlit in one set of observations were sunlit in all the others as well. This reduces the area over which we can effectively map the variation in thermal inertia to the region that appeared in darkness in our observations, roughly corresponding to the trailing hemisphere, to the east of the sub-Mars point.

Another weakness of our model is the assumption it makes that the thermal inertia in each facet is uniform both spatially and with depth. In fact, within each facet, a mixture of particle sizes and rock abundances will result in sub-facet scale hotspots, even into the night. We can only assert that the averaging of many facets within each observation footprint will

make these effects negligible.

The variation of thermal properties with depth is well known in lunar regolith, with lower-density, lower thermal inertia, “fluffy” dust blanketing higher-density, higher thermal inertia subsurface layers (Mitchell et al., 1973; Hayne et al., 2013). A similar stratigraphy could be expected on Phobos, and other authors have included this effect in their thermal modeling (e.g., Bandfield et al. (2018)). However, due to Phobos’ much faster rotational period, the diurnal thermal skin depth of Phobos is much shallower than that of the Moon. As such, our ability to probe the subsurface conditions on Phobos is correspondingly reduced. Therefore we expect the dependence of our observations on this effect to be small, and we have disregarded it in the interest of computational expediency.

### 6.3 Physical Interpretation of Determined Thermal Inertia

In Section 5.1, we find an average thermal inertia of  $42.0 \pm 13.6 \text{ J m}^{-2} \text{ K}^{-1} \text{ s}^{-1/2}$  across the observed portion of Phobos’ surface. How does this compare with other solar system bodies, and what does this allow us to conclude about the physical properties of Phobos’ regolith?

Harris & Drube (2016), and references therein, report thermal inertias for a collection of near-Earth objects (NEOs) and main belt asteroids (MBAs). NEOs generally have thermal inertias greater than  $100 \text{ J m}^{-2} \text{ K}^{-1} \text{ s}^{-1/2}$ , and while MBAs are typically lower, they still generally are greater than  $60 \text{ J m}^{-2} \text{ K}^{-1} \text{ s}^{-1/2}$  or so.

Hayne et al. (2017) provide a high-resolution, detailed map of the thermal inertia of the moon, with a global average of  $\sim 55 \text{ J m}^{-2} \text{ K}^{-1} \text{ s}^{-1/2}$ . Grains in lunar soils range over a few tens to a few hundreds of microns (McKay et al., 1974). It is likely that particles in Phobos’ regolith cover a similar range.

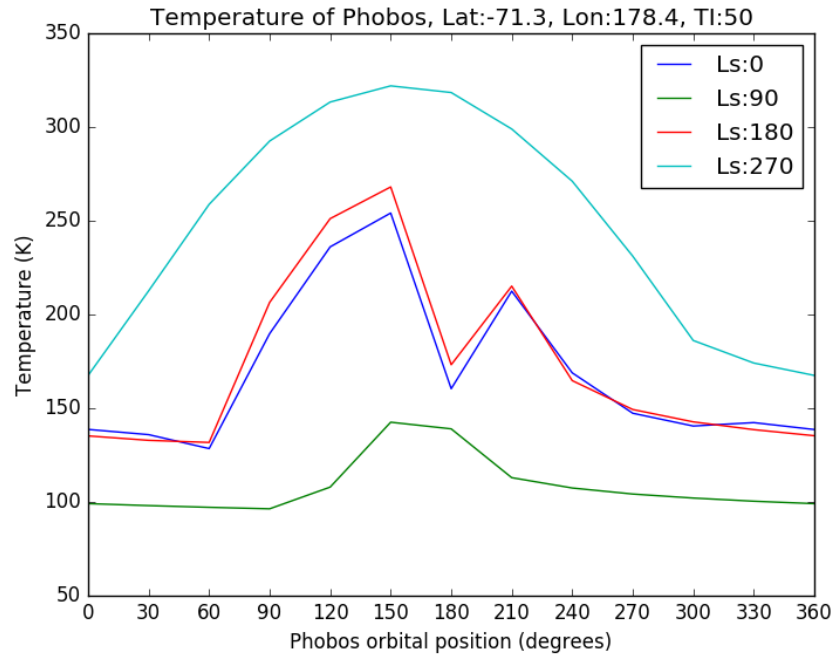


Figure 6.5 Temperature over the course of one orbit for a representative facet near Phobos' southern pole, assuming a thermal inertia of  $50 \text{ J m}^{-2} \text{ K}^{-1} \text{ s}^{-1/2}$ . The four curves each represent one season, at  $L_s = 0, 90, 180,$  and  $270$ . Note that near the Martian equinoxes at  $L_s = 0$  and  $180$ , a large bite is taken out of the afternoon high temperatures, as Phobos enters, and subsequently exits, the shadow of Mars.

## 6.4 Thermal Environment of Phobos

With our average thermal inertia in hand, we can apply our model to a new question: what is the surface temperature of Phobos, and how does it vary both spatially and temporally?

Figure 6.5 illustrates the diurnal temperature curve for a point on Phobos at 4 different times throughout the year. Note that this point is on the Mars-facing hemisphere of Phobos, and so the effects of eclipsing are clearly visible.

Figure 6.6 maps out the temperature extremes experienced on Phobos over the course of one rotation, near perihelion at  $L_s = 270$ .

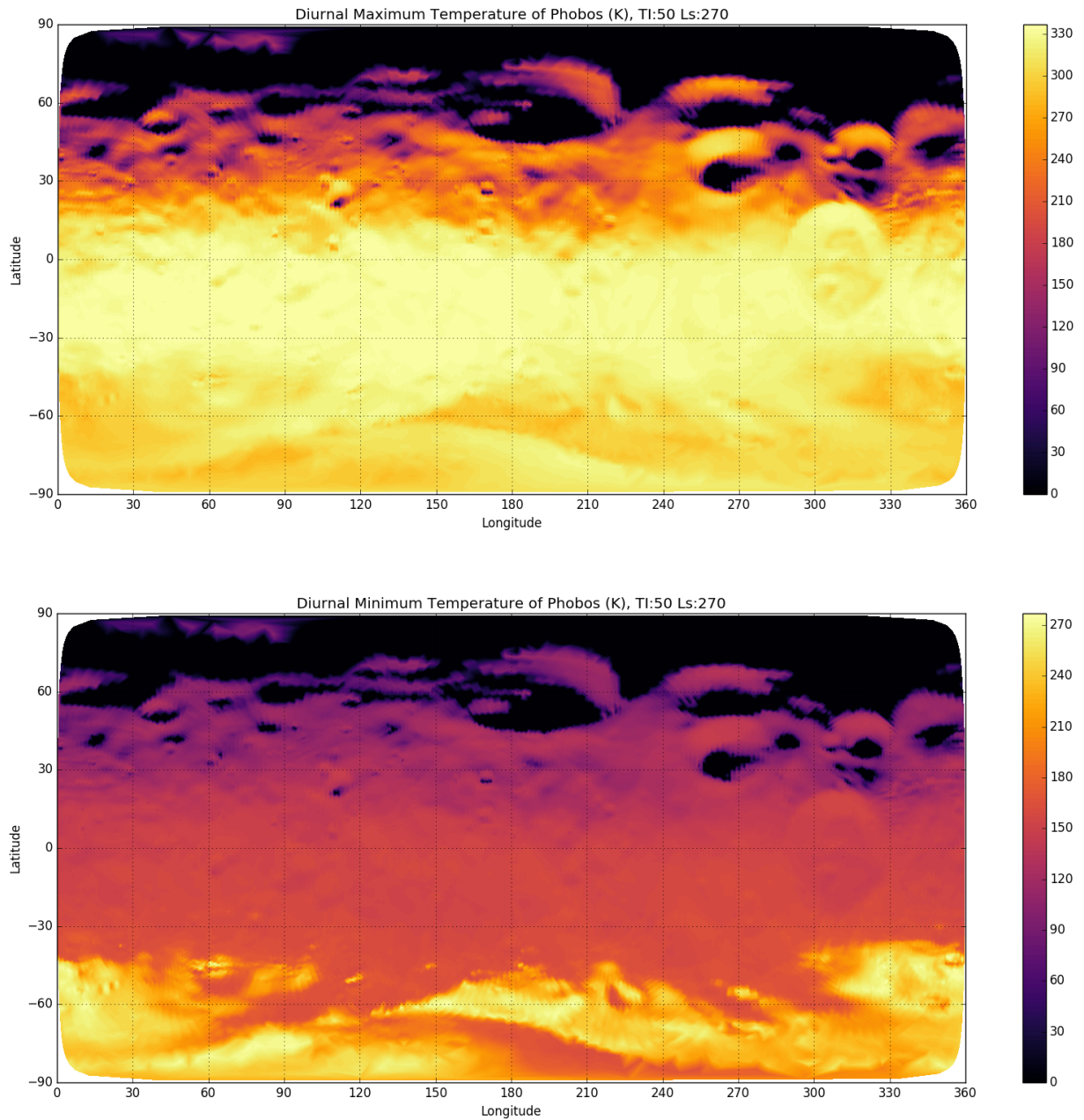


Figure 6.6 Maps showing the maximum (upper) and minimum (lower) temperature of Phobos' surface, over a single orbit at Mars  $L_s = 270$  (near perihelion).

# Chapter 7

## Conclusions and Future Work

### 7.1 Conclusions

In this work we set out to answer the following questions:

1. What is the global average thermal inertia on Phobos?
2. How does thermal inertia vary across Phobos' surface?
3. How do these constraints impact our understanding of Phobos' thermal environment?
4. What do these new constraints imply with regards to the formation of Phobos and the evolution of the Mars system?

We assembled a set of 356 Thermal Emission Spectrometer (TES) observations of Phobos in which Phobos fully filled the TES field of view. We used an airless body thermophysical model, modified for the unique environment of Phobos, to reproduce these observations in simulation. By comparing brightness temperature spectra collected by TES and produced by the model, we were able to find the thermal inertia which best reproduced our observations.

Out of 356 observations, 105 were made at Local Solar Times between 1900 – 0600 LST. Two of these 105 observations were rejected, as they were contaminated by facets near the

south pole that remained illuminated at the time of observation. Of the 103 remaining observations, 94 yielded viable thermal inertias at  $10 \mu\text{m}$ .

Thermal inertias found using these observations averaged  $42.0 \pm 13.6 \text{ J m}^{-2} \text{ K}^{-1} \text{ s}^{-1/2}$ , and ranged from  $16.3 - 97.3 \text{ J m}^{-2} \text{ K}^{-1} \text{ s}^{-1/2}$ , with 90% falling between  $21.7 - 60.6 \text{ J m}^{-2} \text{ K}^{-1} \text{ s}^{-1/2}$ . While individual observations' determined thermal inertias varied, averaging the collection of observations showed that TI varied only moderately across the observed region, suggesting a generally uniform surface. These results successfully provide an answer to questions 1 and 2, above.

Taking the 90% interval of  $\sim 20 - 60 \text{ J m}^{-2} \text{ K}^{-1} \text{ s}^{-1/2}$ , these results are consistent with prior determinations of Phobos' thermal inertia, specifically Kührt et al. (1992)'s  $\sim 20 - 40 \text{ J m}^{-2} \text{ K}^{-1} \text{ s}^{-1/2}$ , and Lunine et al. (1982)'s  $\sim 40 - 70 \text{ J m}^{-2} \text{ K}^{-1} \text{ s}^{-1/2}$ . Importantly, we have also mapped out how thermal inertia varies across Phobos' surface, and have found that it remains fairly uniform across the observed region. This implies an older surface which has had time to come to equilibrium.

The thermal inertia we have identified on Phobos is similar to that of the fine dusty regolith that covers the Moon ( $\sim 50 \text{ J m}^{-2} \text{ K}^{-1} \text{ s}^{-1/2}$ ) (Hayne et al., 2017), suggesting a similar material blankets Phobos as well. Our findings suggest that Phobos changes temperature relatively quickly as illumination conditions change, an important consideration for any visiting spacecraft.

## 7.2 Future Work

A number of potential improvements to our methodology have arisen throughout this project.

The field of view footprints of each observation were identified using an ellipsoid approximation and not the complete shape-model for Phobos. Upgrading this selection process may help to correct some of the issues encountered when modeling observations made just after

sunset.

Developing a method to take into account energy transferred between facets, as well as self-shadowing, will also improve the fidelity of the model. Varying thermophysical properties with depth would increase the complexity of our simulations, but would likely prove to be a more physically accurate approach. Should an improved map of Phobos' albedo become available, the albedo of each facet can be varied independently to further refine our model.

The treatment of Mars as a point illumination source, rather than an extended source, would tend to underestimate the contribution of Mars-shine near Phobos' poles. This may prove an important effect to account for should we undertake an investigation searching for subsurface volatiles trapped in shadowed regions.

We eagerly anticipate any opportunity for new observations of Phobos by new spacecraft, but we would be remiss in continuing to ignore the data which already have been collected by THEMIS on Mars Odyssey and PFS on Mars Express. These data could easily be analyzed using the same methods used here. This could potentially provide a counterpoint to the region observed by TES, which largely focused on the red spectral unit. If the blue spectral unit could be shown to have vastly different thermophysical properties, it would be a highly interesting result.

# Bibliography

- Albee, A. L., Arvidson, R. E., Palluconi, F., & Thorpe, T. 2001, *Journal of Geophysical Research: Planets*, 106, 23291
- Albee, A. L., Palluconi, F., & Arvidson, R. 1998, *Science*, 279, 1671
- Andert, T., Rosenblatt, P., Pätzold, M., et al. 2010, *Geophysical Research Letters*, 37
- Bandfield, J., Piqueux, S., Glotch, T., et al. 2018, in *Lunar and Planetary Science Conference*, Vol. 49
- Bibring, J., Ksanfomality, L., Langevin, I., et al. 1992, *Advances in Space Research*, 12, 13
- Bibring, J.-P., Combes, M., Langevin, Y., et al. 1989, *Nature*, 341, 591
- Bibring, J.-P., Soufflot, A., Berthé, M., et al. 2004, in *Mars Express: the scientific payload*, Vol. 1240, 37–49
- Chase, S. C. 1969, *Applied optics*, 8, 639
- Chase, S. C., Engel, J. L., Eyerly, H. W., et al. 1978, *Applied optics*, 17, 1243
- Christensen, P. R., Bandfield, J. L., Hamilton, V. E., et al. 2001, *Journal of Geophysical Research: Planets*, 106, 23823

- Christensen, P. R., Jakosky, B. M., Kieffer, H. H., et al. 2004, *Space Science Reviews*, 110, 85
- Delbo', M., dell'Oro, A., Harris, A. W., Mottola, S., & Mueller, M. 2007, *Icarus*, 190, 236
- Duxbury, T. C., Zakharov, A. V., Hoffmann, H., & Guinness, E. A. 2014, *Planetary and Space Science*, 102, 9
- Edwards, C., Bandfield, J., Christensen, P., & Fergason, R. 2009, *Journal of Geophysical Research: Planets*, 114
- Formisano, V., Angrilli, F., Arnold, G., et al. 2005, *Planetary and Space Science*, 53, 963
- Fraeman, A., Murchie, S., Arvidson, R., et al. 2014, *Icarus*, 229, 196
- Fraeman, A., Arvidson, R., Murchie, S., et al. 2012, *Journal of Geophysical Research: Planets*, 117
- Gaskell, R. W. 2011, *NASA Planetary Data System*, 154, VO1
- Gatley, I., Kieffer, H., Miner, E., & Neugebauer, G. 1974, *The Astrophysical Journal*, 190, 497
- Giese, B., & Kührt, E. 1990, *Icarus*, 88, 372
- Giuranna, M., Roush, T., Duxbury, T., et al. 2011, *Planetary and Space Science*, 59, 1308
- Hackwell, J. A., Warren, D. W., Chatelain, M. A., et al. 1990, in *Instrumentation in Astronomy VII*, Vol. 1235, International Society for Optics and Photonics, 171–181
- Hall, A. 1877, *The Observatory*, 1, 181
- . 1878, *Monthly Notices of the Royal Astronomical Society*, 38, 205

- Hamilton, V. E., Christensen, P. R., McSween, H. Y., & Bandfield, J. L. 2003, *Meteoritics & Planetary Science*, 38, 871
- Harris, A. W., & Drube, L. 2016, *The Astrophysical Journal*, 832, 127
- Hayne, P., Ghent, R., Bandfield, J., et al. 2013, in *Lunar and Planetary Science Conference*, Vol. 44, 3003
- Hayne, P. O., Bandfield, J. L., Siegler, M. A., et al. 2017, *Journal of Geophysical Research: Planets*
- Iwata, T., Sakanoi, T., Nakagawa, H., et al. 2017, in *Lunar and Planetary Science Conference*, Vol. 48
- Johnston, M., Esposito, P., Alwar, V., et al. 1999, *The strategy for the second phase of aerobraking Mars Global Surveyor*, Tech. rep., NASA Jet Propulsion Laboratory
- Kieffer, H. H., Martin, T., Peterfreund, A. R., et al. 1977, *Journal of Geophysical Research*, 82, 4249
- Ksanfomality, L., Moroz, V., Bibring, J., et al. 1989, *Nature*, 341, 588
- Ksanfomality, L., Murchie, S., Britt, D., et al. 1991, *Planetary and Space Science*, 39, 311
- Kührt, E., & Giese, B. 1989, *Icarus*, 81, 102
- Kührt, E., Giese, B., Keller, H., & Ksanfomality, L. 1992, *Icarus*, 96, 213
- Kuzmin, R., & Zabalueva, E. 2003, *Solar System Research*, 37, 480
- Lagerros, J. S. V. 1996a, *Astronomy and Astrophysics*, 310, 1011
- . 1996b, *Astronomy and Astrophysics*, 315, 625

- . 1997, *Astronomy and Astrophysics*, 325, 1226
- . 1998, *Astronomy and Astrophysics*, 332, 1123
- Lebofsky, L. A., & Spencer, J. R. 1989, in *Asteroids II*, 128–147
- Lewis, S. R., Collins, M., Read, P. L., et al. 1999, *Journal of Geophysical Research: Planets*, 104, 24177
- Lunine, J. I., Neugebauer, G., & Jakosky, B. M. 1982, *Journal of Geophysical Research: Solid Earth*, 87, 10297
- Lynch, D. K., Russell, R. W., Rudy, R. J., et al. 2007, *The Astronomical Journal*, 134, 1459
- Lyons, D. T., Saunders, R. S., & Griffith, D. G. 1995, *Acta Astronautica*, 35, 669
- McKay, D., Fruland, R., & Heiken, G. 1974, in *Lunar and Planetary Science Conference Proceedings*, Vol. 5, 887–906
- Mellon, M. T., Jakosky, B. M., Kieffer, H. H., & Christensen, P. R. 2000, *Icarus*, 148, 437
- Millour, E., Forget, F., Spiga, A., et al. 2015, in *European Planetary Science Congress 2015*, Vol. 10, EPSC, EPSC2015–438
- Mitchell, J., Carrier III, W., Costes, N., Houston, W., & Scott, R. 1973, in *Lunar and Planetary Science Conference Proceedings*, Vol. 4, 2437
- Mommert, M., Farnocchia, D., Hora, J. L., et al. 2014a, *The Astrophysical Journal Letters*, 789, L22
- Mommert, M., Hora, J., Farnocchia, D., et al. 2014b, *The Astrophysical Journal*, 786, 148
- Mueller, M. 2007, PhD thesis, Freie Universität Berlin, arXiv:1208.3993

- Müller, T., Sterzik, M., Schütz, O., Pravec, P., & Siebenmorgen, R. 2004, *Astronomy & Astrophysics*, 424, 1075
- Murchie, S., & Erard, S. 1996, *Icarus*, 123, 63
- Murchie, S., Arvidson, R., Bedini, P., et al. 2007, *Journal of Geophysical Research: Planets*, 112
- Murchie, S., Choo, T., Humm, D., et al. 2008, in *Lunar and Planetary Science Conference*, Vol. 39, 1434
- Petty, G. W. 2006, *A first course in atmospheric radiation*, 2nd edn. (Sundog Publishing)
- Pieters, C. M., Murchie, S., Thomas, N., & Britt, D. 2014, *Planetary and space science*, 102, 144
- Pratt, W., & Hopkins, J. 2011, in *AIAA SPACE 2011 Conference & Exposition*, 7140
- Putzig, N. E. 2006, PhD thesis, University of Colorado at Boulder
- Rivkin, A., Brown, R., Trilling, D., Bell III, J., & Plassmann, J. 2002, *Icarus*, 156, 64
- Sagdeev, R., & Zakharov, A. 1989, *Nature*, 341, 581
- Selivanov, A., Naraeva, M., Panfilov, A., et al. 1989, *Nature*, 341, 593
- Shure, M. A., Toomey, D. W., Rayner, J. T., Onaka, P. M., & Denault, A. J. 1994, in *Instrumentation in Astronomy VIII*, Vol. 2198, International Society for Optics and Photonics, 614–623
- Smith, M. D., Bandfield, J. L., & Christensen, P. R. 2000, *Journal of Geophysical Research: Planets*, 105, 9589
- Spencer, J. R. 1990, *Icarus*, 83, 27

Stooke, P. 2015, NASA Planetary Data System

Thomas, P., Veverka, J., Sullivan, R., et al. 2000, *Journal of Geophysical Research: Planets*, 105, 15091

Toomey, D. W., Ftaclas, C., Brown, R. H., & Trilling, D. 1998, in *Infrared Astronomical Instrumentation*, Vol. 3354, International Society for Optics and Photonics, 782–791

Wang, S.-i., Owensby, P. D., Toomey, D. W., et al. 1994, in *Instrumentation in Astronomy VIII*, Vol. 2198, International Society for Optics and Photonics, 578–590

Willner, K., Shi, X., & Oberst, J. 2014, *Planetary and Space Science*, 102, 51

Witasse, O., Duxbury, T., Chicarro, A., et al. 2014, *Planetary and Space Science*, 102, 18

# Appendix A

## Mars-Shine

### A.1 Overview

This project was undertaken to improve the accuracy of a thermophysical model of Phobos. For purposes of thermal modeling of the Martian satellites, the relevant quantities are the infrared thermal flux arriving at the moon, and the visible scattered flux arriving at the moon.

These two fluxes depend on the apparent size of Mars in the sky over the moon, and the amount of radiation of each type leaving the Martian surface. Mars' apparent size can be calculated from simple geometry. While using a blackbody-radiation model could offer a simple route to determining the thermal emission from Mars' surface, I opted to apply a Mars global climate model to the problem. The Mars Climate Database (MCD) (Lewis et al., 1999; Millour et al., 2015), developed and hosted at the Laboratoire de Météorologie Dynamique (LMD) in Paris, can be queried for any point on Mars, at any hour and season, to return both the thermally emitted and solar scattered flux at that point.

In order to relate the flux leaving points on Mars' surface to the flux arriving at a moon, the departing flux must first be converted to a radiant intensity, or flux per unit solid angle.

Intensity is conserved along any transparent optical path. This is in contrast with flux, which diminishes with distance by  $1/r^2$ . This property is easily demonstrated by imagining a well-lit sheet of paper in a dark room. While the total flux shrinks as you back away from the paper, the sheet always appears the same brightness; it is the shrinking apparent size of the paper which results in the diminishing flux.

It would be too simple to apply a single intensity to the whole apparent disk of Mars, as the albedo and surface temperature would surely vary across the observed region, which covered an area over  $120^\circ$  across in longitude and latitude. Instead, I randomly generated 3000 points on Mars, selected evenly in angular space from the perspective of Phobos. These points were then queried for their fluxes to space. The flux departing each point was converted to a radiant intensity. Finally, each radiant intensity was multiplied by  $1/3000$ th of the total solid angle subtended by Mars, and then summed to find the total Mars-shine flux arriving at Phobos.

A more thorough description of this process follows in the sections below.

## A.2 Apparent size of Mars

The apparent size of Mars, or, more precisely, the solid angle  $\Omega$  subtended by Mars, depends on the distance  $d$  from Mars' center, and the radius of Mars,  $r_m$ . Phobos' true orbit has a 9378 km semi-major axis, an eccentricity  $e$  of 0.0151, and an inclination with respect to Mars' equator  $i$  of  $1.08^\circ$ . For simplicity, we assume Phobos to have a perfectly circular ( $e = 0$ ) and equatorial ( $i = 0^\circ$ ) orbit with  $d = 9378$  km. We also assume Mars to be a sphere with  $r_m = 3396.2$  km. The effects of these simplifying assumptions on our resulting determination of Mars-shine are negligible.

From these two measurements, we can determine Mars' angular radius,  $\theta$ . As Fig. A.1 makes clear, the line of sight from Phobos to Mars' limb must meet Mars' radius at a right

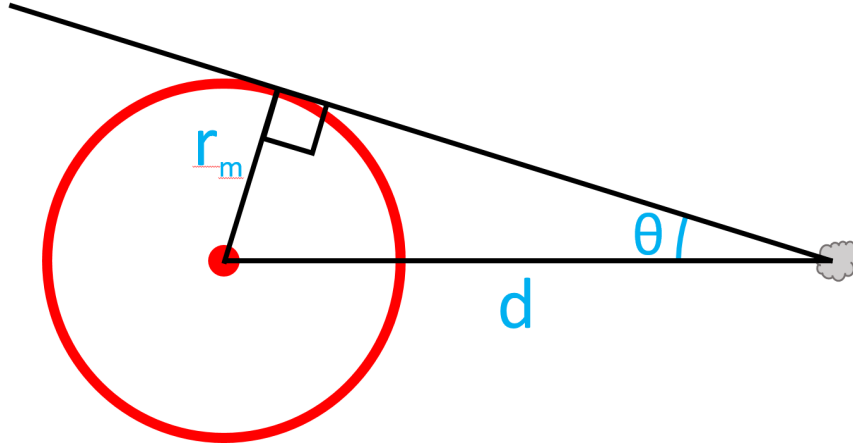


Figure A.1 Defining several key variables.  $r_m$  is the radius of Mars,  $d$  is the distance to Phobos' orbit, and  $\theta$  is the apparent angle between the center of Mars and its limb, viewed from Phobos (i.e., Mars' angular radius).

angle. Therefore we can determine  $\theta$  by the trigonometric relationship in equation A.1:

$$\theta = \sin^{-1}\left(\frac{r_m}{d}\right) \quad (\text{A.1})$$

To find the solid angle subtended by a sphere, we first define a cone with its apex at the observer and sides that pass tangent to the surface of the sphere. The cone then intersects a sphere centered on the observer, forming a spherical cap, as seen in Fig. A.2. It is the surface area of this spherical cap that, for a unit sphere, gives us the solid angle we desire. The formula for the solid angle is therefore given by equation A.2.

$$\Omega = 2\pi(1 - \cos \theta) \quad (\text{A.2})$$

For Phobos, we can input  $r_m$  and  $d$  into equation A.1 and we find  $\theta = 21.2^\circ$ . We then input this  $\theta$  into equation A.2 and find  $\Omega = 0.4265$  steradians.

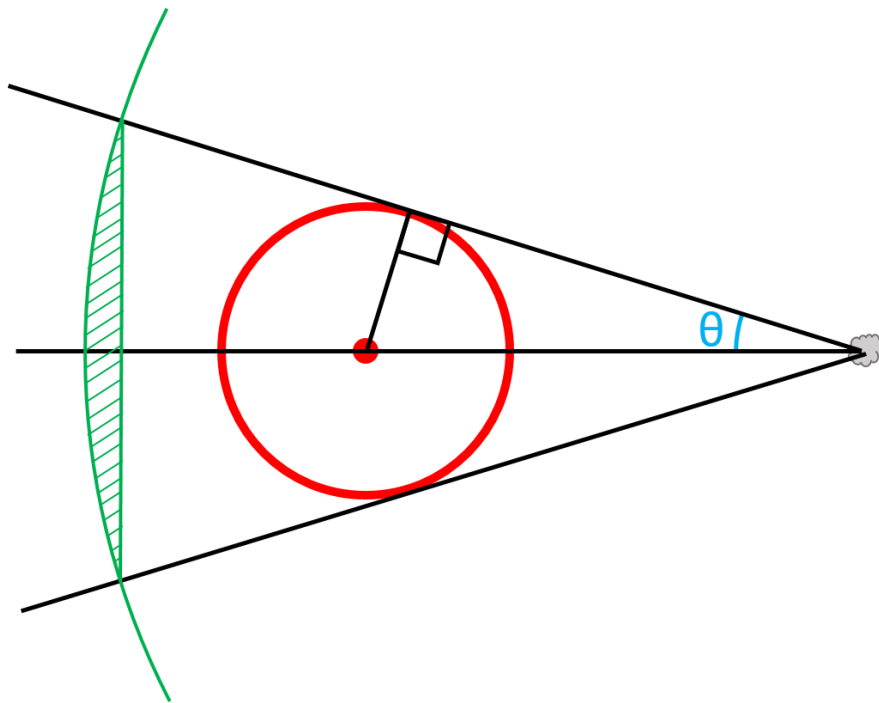


Figure A.2 Defining a spherical cap. The cap (hashed green) is the intersection of a sphere centered on the observer (green) and a cone (black) with apex angle  $2\theta$ . For a unit sphere, the surface area of this spherical cap is equal to the solid angle subtended by the cone, which in turn is equal to the solid angle subtended by the red sphere, representing Mars.

## A.3 Mars global climate model

The LMD Mars Climate Database is a rigorous global climate model for engineering and scientific purposes developed for mission planning and analysis of observations. It has been validated using atmospheric and surface observations from Mars Global Surveyor, Mars Express, the Viking, Pathfinder, and Phoenix landers, and the Curiosity rover. It can model global dust storms, atmospheric convection, the water cycle, and much more.

To use the MCD, several interfaces are offered, including a web-browser GUI. For heavier computation, one can operate the MCD using Fortran, C, and Python. I elected to use the Python interface.

When calling the MCD from Python, you must specify a number of input variables, including the latitude and longitude of interest, the global dust condition, Mars solar longitude ( $L_s$ ), and local solar time. Relevant to this work are two output variables: Solar flux to space and thermal IR flux to space. These outputs give the power per unit area ( $W/m^2$ ) being scattered or thermally emitted by the surface at a given point which makes it out of the atmosphere.

## A.4 Radiant intensity

We assume for simplicity the flux leaving a location on Mars' surface is scattered or emitted isotropically. This means that the fluxes to space from the MCD must be divided into the whole sky to find the radiant intensity, or flux per unit solid angle traveling in some direction  $\hat{\Omega}$ . The sky occupies a hemisphere, or  $2\pi$  steradians of solid angle.

However, intensity is formally defined in Petty (2006), section 2.7.2 as

$$I(\hat{\Omega}) = \frac{\delta F}{\delta \omega} \quad (\text{Petty, 2.51})$$

and so, to evaluate flux, we must integrate  $I(\hat{\Omega})d\omega$  over  $2\pi$  steradians. Helpfully, our emission and scattering is assumed to be isotropic. In this case, Petty evaluates this integral for us, giving

$$F = \pi I \tag{Petty, 2.60}$$

Thus, to find the radiant intensity from a location on Mars, we must divide our flux by  $\pi$ , and not by  $2\pi$ .

## A.5 Statistical integration

In order to capture the variability in surface conditions across the observed region of Mars, I devised a strategy to integrate the radiant intensity over the entire area. Recall the formal definition of intensity given above, in equation Petty, 2.51. By rearranging we can solve for flux:

$$F = \int I(\hat{\Omega})\delta\omega \tag{A.3}$$

The dependence of  $I$  on  $\hat{\Omega}$  tells us that while the incident flux is measured passing through a reference surface, intensity is defined along a direction at some incidence angle  $\theta_i$  from the normal to that surface. As such we must include a  $\cos(\theta_i)$  term in our final evaluation.

In order to evaluate this integral analytically, we would need a functional expression of the intensity in angular space. However, we can instead evaluate flux numerically. By dividing the observed region of Mars into small solid angle elements  $\delta\omega$ , we find the corresponding intensities, multiply, and sum each element to integrate the total flux.

$$F = \sum I \cos(\theta_i)\delta\omega \tag{A.4}$$

But, dividing the observed region into solid angle elements is non-trivial, given Mars' curva-

ture. Even simpler than a strict numerical integration was a Monte Carlo-inspired “statistical integration”.

To perform this statistical integration, I first needed to randomly select a large number  $N$  points on the surface of Mars, while keeping my selection unbiased in angular space as viewed from Phobos. Next, for each point, I queried the MCD to find the flux leaving the surface to space. By dividing by  $\pi$ , I converted each flux to intensity. I assigned each surface location a small solid angle element  $\delta\omega$  equal to  $1/N$  times the total solid angle  $\Omega$  subtended by Mars. From that point, finding  $F$  was as simple as multiplying each  $\delta\omega$  by its corresponding  $I$  and  $\cos(\theta_i)$ , and summing everything up. With a large enough  $N$ , this approximation of a rigorous numerical integration converges on the same result.

### A.5.1 Selection of points

In order for this method to work, points on Mars’ surface need to be selected evenly in angular space from Phobos. Unlike sampling evenly in surface area, selecting latitude-longitude pairs on one body conforming to the angular space of another will necessitate a more complex solution. My method involves casting rays out from Phobos, and finding those that intersect with Mars’ surface.

First, we place Phobos in some position along its orbit using Cartesian Mars-centered coordinates. Next, we generate random unit vectors evenly around all angles; that means latitudes from 0 to  $\pi^1$ , and longitudes from 0 to  $2\pi$ . We convert those unit vectors from spherical coordinates to Cartesian. We multiply them by the distance,  $h$ , from Phobos to Phobos’ Mars horizon. Recalling figure A.1, we can see  $h$  is the third side of the right triangle

---

<sup>1</sup>Note that in selecting random latitudes, one cannot simply pull from a uniform distribution on 0 to  $\pi$ , as this will over-sample the poles, where each ring of  $\delta\phi$  will have ever-smaller area. The correct method is to select a random number sampled uniformly on  $-1$  to  $1$ , then set the latitude to be the arccosine of this random number.

formed by  $r_m$  and  $d$ , and so we find  $h$  as follows:

$$h = \sqrt{d^2 + r_m^2} \quad (\text{A.5})$$

We now have vectors of length  $h$  pointing in all directions. We then add them to Phobos' position vector, essentially casting rays in all directions from Phobos.

Now, we check if the resulting point is within  $1 r_m$  from the origin (i.e., the center of mars). Consider the spherical shell of all possible vectors of length  $h$  we have now cast. All and only those vectors which intersect with Mars' surface will end inside  $1 r_m$ . If the random vector we have produced does not, we can now repeat the procedure until we find one that does.

To determine the intersection  $(x, y, z)$  of the vector and Mars' surface, we solve a set of two equations. The first describes the line between Phobos ( $p$ ) and the point  $v$  at the end of the vector:

$$[x, y, z] = [x_p, y_p, z_p] + t[x_v, y_v, z_v] \quad (\text{A.6})$$

where  $t$  is a scaling factor. The other equation describes the surface of an origin-centered sphere with radius  $r_m$ :

$$x^2 + y^2 + z^2 = r_m^2 \quad (\text{A.7})$$

First, we can decompose equation A.6 to solve for the components  $x$ ,  $y$ , and  $z$  independently:

$$x = x_p + t(x_v - x_p) \quad (\text{A.8})$$

$$y = y_p + t(y_v - y_p) \quad (\text{A.9})$$

$$z = z_p + t(z_v - z_p) \quad (\text{A.10})$$

This gives us four equations (A.7, A.8, A.9, A.10), and four unknowns,  $x$ ,  $y$ ,  $z$ , and  $t$ . Solving the system involves substituting in for  $x$ ,  $y$ , and  $z$  in equation A.7, yielding:

$$(x_p + t(x_v - x_p))^2 + (x_p + t(y_v - y_p))^2 + (x_p + t(z_v - z_p))^2 = r_m^2 \quad (\text{A.11})$$

Solving equation A.11 for  $t$  produces the following:

$$t = \frac{A \pm \frac{1}{2}[(2A)^2 + 4B(r_m^2 - x_p^2 - y_p^2 - z_p^2)]^{\frac{1}{2}}}{B} \quad (\text{A.12})$$

where  $A$  is defined as:

$$A = (x_p^2 - x_p x_v + y_p^2 - y_p y_v + z_p^2 - z_p z_v) \quad (\text{A.13})$$

and  $B$  is defined as:

$$B = (x_p^2 - 2x_p x_v + x_v^2 + y_p^2 - 2y_p y_v + y_v^2 + z_p^2 - 2z_p z_v + z_v^2) \quad (\text{A.14})$$

Due to the  $\pm$ , there are two solutions to equation A.12. This corresponds to the line passing through the sphere and intersecting the opposite surface. Therefore the solution we desire is always the smaller  $t$ . Once  $t$  has been found, it can be substituted into equations A.8, A.9, and A.10 to find  $x$ ,  $y$ , and  $z$ . This gives us the point of intersection between the sphere and line, and thus, the Cartesian coordinates of a point on Mars' surface selected randomly in angular space.

Now we convert that Cartesian point to a latitude, longitude, and radius. As an extra sanity check, we can confirm the radius is  $r_m$ .

The above procedure can be repeated to collect as many points as desired. I found 3000 points to be sufficient to produce results which results that remained consistent upon

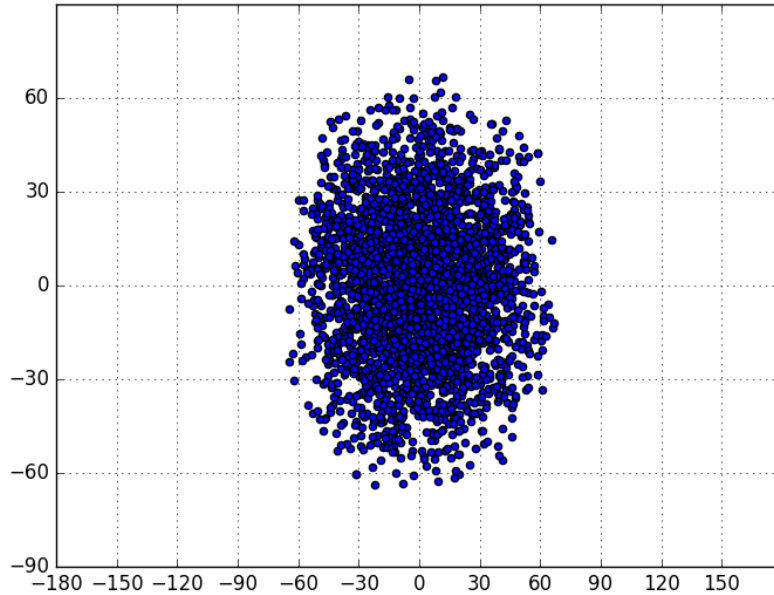


Figure A.3 A collection of 3000 points on the surface of Mars, sampled randomly in angular space as viewed from Phobos. This global map of Mars is shown with latitude on the y-axis, ranging from  $-90^\circ$  to  $+90^\circ$ , and longitude on the x-axis, ranging from  $-180^\circ$  to  $+180^\circ$ . The arbitrary rectangular map projection distorts the true appearance of the circular region. Points are clustered toward the center of the region when mapped in this way, but when viewed from Phobos, these points would appear to have a constant density across Mars' apparent disk.

repetition. Figure A.3 is an example collection of points. Note how in latitude-longitude space, the points are clustered toward the center of the region, with fewer near the margins.

## A.5.2 Local time

Each query to the MCD needed to specify the true local solar time at the point of interest as a decimal Mars hour (i.e.,  $\frac{1}{24}$  of a Mars sol). At any given moment, points in the eastern portion of the observed region would have a later true local solar time than their counterparts in the west. In order to properly add together all the flux which would arrive at Phobos at

a certain time, the queried time would have to be adjusted according to a point's longitude. This longitude corrected time would have the form:

$$T_{\text{corrected}} = T_{\text{center}} + (\lambda_{\text{center}} - \lambda_{\text{point}}) \frac{24\text{h}}{360^\circ} \quad (\text{A.15})$$

where  $T_{\text{corrected}}$  is the corrected time,  $T_{\text{center}}$  is the time at the center of the observed region (i.e., the sub-Phobos point),  $\lambda_{\text{center}}$  is the longitude at the center of the observed region, and  $\lambda_{\text{point}}$  is the longitude of the point of interest. The factor of  $(24\text{h}/360^\circ)$  converts the longitude difference (in degrees) to a time offset (in hours of local time). In this way, all points in the observed region were queried for times that were simultaneous, corresponding to the clock at the sub-Phobos point.

## A.6 Results

I repeated the above procedure for 25 local solar time hours for 12 different positions of Phobos around Mars for each  $L_s$  of interest (0, 90, 180, 270, perihelion, aphelion, and the  $L_s$  corresponding to each of three sets of Phobos observations, for a total of 9  $L_s$  so far). I arranged the 25 local solar time hours into a diurnal curve. Finally I averaged together the 12 diurnal curves corresponding to each position around Mars, in order to eliminate the effects of local features. This was necessary because Phobos orbits Mars every 7.65 hours, with Mars rotating every 24.6 hours, making it difficult to implement a scheme to feed to my thermal model the Mars-shine flux corresponding to the correct illumination for the correct region of Mars.

One such average is seen in Figure A.4. Fortunately, the average diurnal curve well represents the behavior across Mars. Residuals between individual regions' diurnal curves and the average are low, only 1-2  $\text{W}/\text{m}^2$ , as shown in Figure A.5.

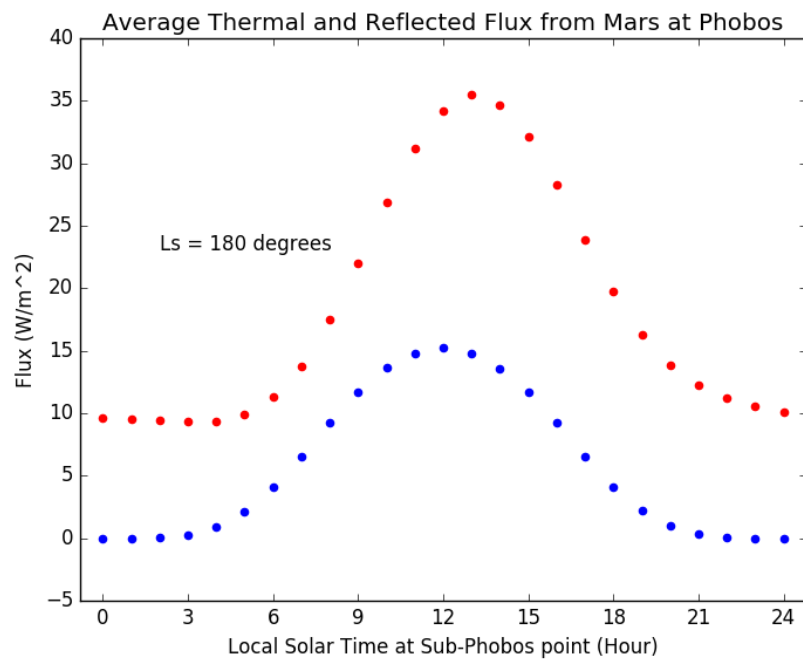


Figure A.4 A diurnal Mars-shine curve. Red points indicated thermal emission, blue points are scattered solar light. This is an average of 12 curves collected from different positions over Mars, which is to say different positions in Phobos' orbit.

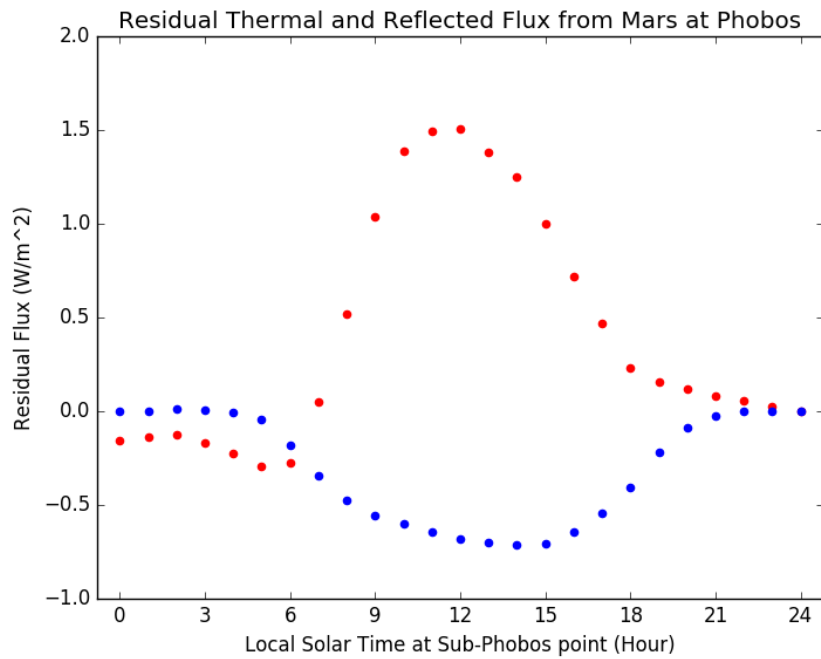


Figure A.5 Residuals from the averaged diurnal curve for Mars-shine at  $L_s = 180$ . Residuals are consistently small, typically less than  $2 \text{ W/m}^2$ . Red points indicated thermal emission, blue points are scattered solar light. The shape of this curve is due to the albedo and thermal inertia of the surface in the observed region of Mars. A low albedo feature in the region led to lower visible reflected light during the day, more absorption, higher temperatures, and thus more thermal emission.

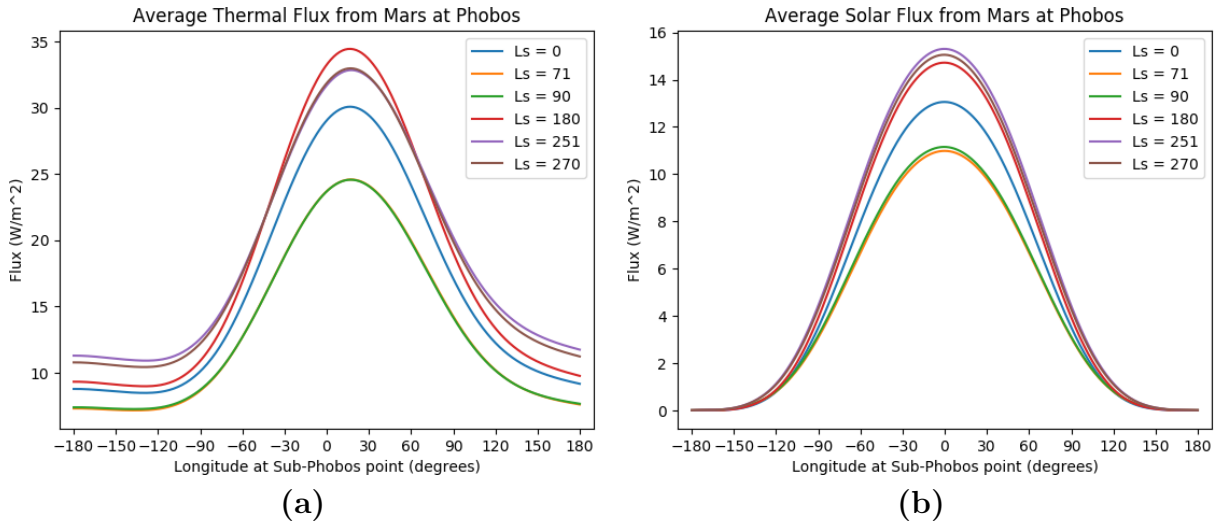


Figure A.6 **(a)** Average diurnal curve of thermal IR Mars-shine for four seasons, plus aphelion and perihelion. Peak emission ranges from  $\sim 35 - 25 \text{ W/m}^2$ , depending on season. **(b)** Average diurnal curve of solar Mars-shine for four seasons, plus aphelion and perihelion. Peak scattered light ranges from  $\sim 15.5 - 11 \text{ W/m}^2$ , depending on season.

I then fit the averages to a function using a cubic spline interpolation. This allows Mars-shine to be added into my thermophysical model as an illumination source. Average thermal and solar components for  $L_s = 0, 90, 180,$  and  $270$  are shown in figure A.6.